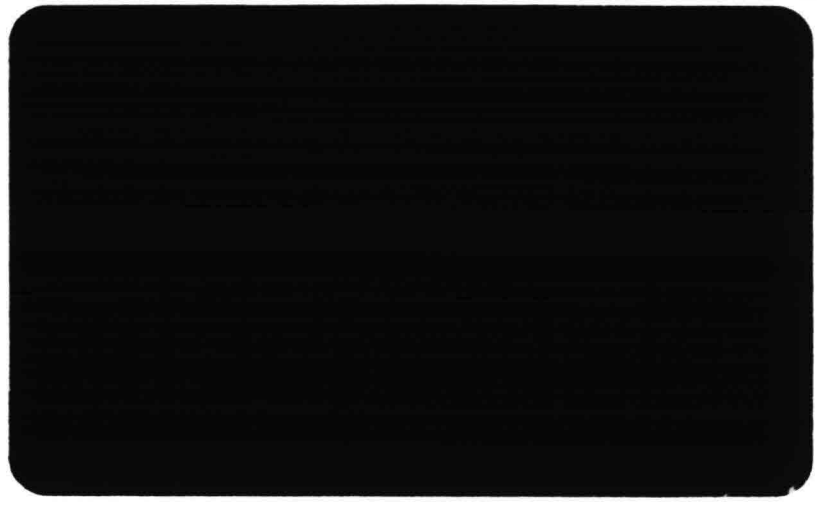

TU Delft
Delft University of Technology

Department of Civil Engineering
Hydraulic and Geotechnical Engineering Division
Hydromechanics Section

Recirculating steady flow in harbours: comparison of numerical computations to laboratory measurements

M.D.J.P. Bijvelds
report no. 1-97

1997

The work reported herein has been made possible by financial support of RIKZ, Rijkswaterstaat

TU Delft

Ph.D. student, Hydromechanics Section, Faculty of Civil Engineering and Geosciences, Delft University of Technology, P.O. Box 5048, 2600 GA, the Netherlands. Tel. +31 15 278 44 64; Fax +31 15 278 59 75; E-mail: M.Bijvelds@ct.tudelft.nl

Abstract

In this report the water flow in harbours, that are situated on a river, are considered. Due to the flow velocity difference between the river and the harbour, a turbulent mixing layer develops at the harbour entrance. The shallowness of the water induces the coexistance of two disparate turbulent length scales in these regions. Besides the "ordinary" small-scale 3D turbulence, which is generated by bottom friction, large quasi 2D turbulent structures are generated by horizontal shear in the mixing layer. These large structures have a typical turbulent length scale that, in contrast with the 3D turbulence, is at least several times the water depth.

The standard 3D k-ε turbulence model, takes only one turbulent length scale into account and, as a consequence, the computed eddy viscosities and Reynolds stresses are too low, which results in an underprediction of the velocities in the gyre. Therefore, a new turbulence model, based on the standard k-ε turbulence model, was developed that does take non-isotropic behaviour of the turbulence into account. This new model consists of two distinct turbulence models, that together model the 3D and quasi-2D turbulence: the vertical eddy viscosity that determines the vertical Reynolds stresses are computed with a 3D k-ε turbulence model, in which the production of turbulent kinetic energy is determined by vertical shear only, i.e. bottom friction. The horizontal eddy viscosity that determines the horizontal Reynolds stresses is computed by a 2D depth averaged k-ε model, in which the production of turbulent kinetic energy is dependent upon horizontal velocity gradients only. Direct interaction between the two turbulence models, by means of energy transfer, is neglected. However, interaction via the mean-flow equations still exists.

The standard 3D k-ε turbulence model and the new two-length-scale model were tested for two different geometries. Besides earlier measurements in a 1x1 m^2 harbour, new measurements that were carried out in a more realistic geometry were used for model testing. The laser Doppler experiments carried out in the latter scale model, clearly revealed the existance of two disparate turbulent length scales by studying the autocorrelation functions and the turbulent power density spectra at positions in the mixing layer and the river. In both cases, results from computations with the two-length-scale model were in better agreement with measurements than the standard one-length-scale k-ε model, supporting the necessity to account for the non-istropy of the turbulence.

Contents

1 Introduction **3**

2 A two-length-scale k-ε turbulence model **5**
2.1 The standard k-ε turbulence model 5
2.2 A depth-averaged k-ε model for determining ν_t^{2D} 7
2.2.1 Introduction 7
2.2.2 Theoretical background 7
2.2.3 Model equations 11
2.2.4 Numerical aspects 13

3 Laboratory measurements **15**
3.1 Experimental set up 15
3.1.1 Scale model of yacht harbour "'t Steel" 15
3.1.2 Measuring equipment 17
3.2 Results of measurements 20

4 Modelling recirculating harbour flow **26**
4.1 Cavity driven flow in a square model harbour 26
4.1.1 Model description 26
4.1.2 Results 27
4.2 Modelling yacht harbour "'t Steel" 30
4.2.1 Results 30

5 Conclusions and recommendations **34**

References **38**

List of Figures **40**

Figures **43**

Chapter 1

Introduction

Harbours situated on rivers and estuaries usually suffer from siltation of their basins. The routine dredging necessary to sustain the accessibility of the harbour to shipping, and the disposal of the mostly polluted sediment, involve high costs.

The siltation is induced by the flow at the harbour entrance which is influenced by gyres, changes in water level, density currents and the geometry of the harbour. As a result, the water motion in the harbour entrance is complex and of a three-dimensional nature. Detailed knowledge of the water motion is imperative for a reliable prediction of transport of matter in general and the siltation of harbours in particular. However, too little is known of the complex flow in the harbour entrance to reliably predict the siltation of harbour basins at present.

The velocity difference between the river and the harbour produces a turbulent mixing layer transferring momentum from the river into the harbour. This momentum transfer gives rise to a recirculating flow in the harbour. The gyre which develops in a square harbour is mainly two-dimensional and can be successfully simulated by depth averaged numerical models that use a constant eddy viscosity coefficient the value of which is based on the turbulence properties in the mixing layer between harbour and river (Langendoen & Kranenburg, 1993) or on a depth averaged k-ε turbulence model (Booij, 1989). However, because of their nature, these models fail to represent three-dimensional properties of the flow and are therefore a priori unable to predict siltation.

In general, the flow in harbours can be considered as shallow-water flow, which means that horizontal length scales of the flow are much larger than vertical length scales. Under these conditions, a shallow mixing layer develops and the width of this mixing layer can extend to several times the local water depth (Uijttewaal & Tukker, 1997), (Tukker, 1997). This means that the largest turbulent structures that exist in the mixing layer have a (quasi) two-dimensional character. In this situation, two turbulent length scales can be distinguished. Firstly, turbulence generated by bottom friction is of three-dimensional nature and the associated length scale is of the order of the water depth. Secondly, larger turbulent structures related to the horizontal shear in the mixing layer and gyre exist and are (quasi-) two-dimensional. The quasi two-dimensional character impedes the cascade process related to vortex stretching. Energy is transferred directly to the small turbulent scales, without the

intervention of a continuum of intermediate scales (Babarutsi & Chu, 1991).

The co-existence of two characteristic turbulent length scales makes the application of the standard three-dimensional k-ε turbulence model in numerical simulations inadequate. In order to obtain reasonable results, the non-isotropic behaviour of the flow should be reflected in the turbulence model used. In chapter 2 a two-length-scale turbulence model, based on the standard k-ε model, is presented, that accounts for this behaviour of the turbulence. This model is shown to perform better than the standard k-ε model.

Although a number of studies on the exchange through the mixing layer have been reported (Rohr, 1933), (Vollmers, 1963), (Dursthoff, 1970), (Westrich, 1977) and (Booij, 1986), adequate data to test numerical models is still missing for realistic geometries. In chapter 3 measurements concerning the flow in a scale model of a harbour on the river Meuse, is presented.

In chapter 4 results from numerical computations are compared to laboratory measurements. Besides the abovementioned situation, earlier laboratory measurements of the flow in a square harbour of 1 x 1 m^2 (Langendoen, 1992), driven by an adjacent river are used for comparison. In both cases the flow is stationary and homogeneous, which means that the only driving force for the circulation in the harbour is the momentum transfer from river to harbour in the mixing layer. Finally conclusions and recommendations for further research are presented.

Chapter 2

A two-length-scale k-ε turbulence model

The two-length-scale (TLS) turbulence model was implemented in the Delft Hydraulics hydrodynamic program TRISULA (Delft Hydraulics, 1994), which among other things, contains a modified version of the standard three-dimensional k-ε model (Rodi, 1980). In the following sections, this model and the new TLS turbulence model are discussed.

2.1 The standard k-ε turbulence model

The numerical model TRISULA (Delft Hydraulics, 1994) comprises approximations for continuity, momentum and transport equations for quantities such turbulent kinetic energy (TKE) k and its dissipation rate ε. The momentum equations are based upon the hydrostatic pressure assumption and in Cartesian coordinates given by:
continuity equation:

$$\frac{\partial u_i}{\partial x_i} = 0 \tag{2.1}$$

momentum equation:

$$\frac{\partial u_i}{\partial t} + u_j \frac{\partial u_i}{\partial x_j} + \frac{1}{\rho}\frac{\partial p}{\partial x_i} - \frac{1}{\rho}\frac{\partial \tau_{ij}}{\partial x_j} = f_i, \quad i = 1,2 \tag{2.2}$$

hydrostatic pressure assumption:

$$\frac{\partial p}{\partial x_3} = -\rho g \tag{2.3}$$

transport equations:

$$\frac{\partial c}{\partial t} + \frac{\partial F_i}{\partial x_i} = S \tag{2.4}$$

where u_i is the velocity in the x_i direction. p is the pressure. ρ is the density. τ_{ij} is the Reynolds stress tensor, g is the acceleration due to gravity. c is the concentration. f_i is an external forcing. F_i is the concentration flux due to convection and diffusion and S is a source term.

The Reynolds stress tensor τ_{ij} is modelled by introducing the Boussinesq hypothesis:

$$-\tau_{xz} = \rho\nu_t^v \left(\frac{\partial u}{\partial z}\right), \quad -\tau_{yz} = \rho\nu_t^v \left(\frac{\partial v}{\partial z}\right) \tag{2.5a}$$

$$-\tau_{xx} = 2\rho\nu_t^h \left(\frac{\partial u}{\partial x}\right), \quad -\tau_{yy} = 2\rho\nu_t^h \left(\frac{\partial v}{\partial y}\right), \quad -\tau_{xy} = -\tau_{yx} = \rho\nu_t^h \left(\frac{\partial u}{\partial y} + \frac{\partial v}{\partial x}\right) \tag{2.5b}$$

In these equations x and y are horizontal coordinates and z is the vertical coordinate. Note that, in agreement with the boundary layer approximation, some elements of the full three-dimensional Reynolds stress tensor and deformation tensor have been neglected. In eq. (2.5a) and (2.5b) different eddy viscosities are used. Reynolds stresses which transfer momentum in the vertical direction are modelled by using a vertical eddy viscosity ν_t^v and the Reynolds stresses which transfer momentum in the horizontal direction are modelled by using a horizontal eddy viscosity ν_t^h. The latter is assumed to be a superposition of two parts: a part due to "2D turbulence" and a part due to "3D turbulence" (Uittenbogaard *et al.*, 1992)

$$\nu_t^h = \nu_t^{2D} + \nu_t^v \tag{2.6}$$

The 3D part is determined by a turbulence model, while in the original TRISULA formulationthe 2D part must be specified by the user. This way directional dependency is introduced in the turbulence model.

In the k-ε turbulence model, both the TKE k and the dissipation rate ε of TKE are computed by solving transport equations for these quantities. The vertical eddy viscosity is calculated from these turbulent quantities by defining

$$\nu_t^v = c_\mu \frac{k^2}{\varepsilon} \tag{2.7}$$

where c_μ is a model coefficient. The transport equations for k and ε, in case of uniform density, are given by

$$\frac{\mathrm{D}k}{\mathrm{D}t} = \frac{\partial}{\partial z}\left(D_v \frac{\partial k}{\partial z}\right) + P_k - \varepsilon \tag{2.8a}$$

$$\frac{\mathrm{D}\varepsilon}{\mathrm{D}t} = \frac{\partial}{\partial z}\left(D_v \frac{\partial \varepsilon}{\partial z}\right) + P_\varepsilon - c_{2\varepsilon}\frac{\varepsilon^2}{k} \tag{2.8b}$$

where $\mathrm{D}/\mathrm{D}t = \partial/\partial t + u\partial/\partial x + v\partial/\partial y + w\partial/\partial z$ is the material derivative. The production terms P_k and P_ε are defined by

$$P_k = \nu_t^v \left[\left(\frac{\partial u}{\partial z}\right)^2 + \left(\frac{\partial v}{\partial z}\right)^2\right] \tag{2.9a}$$

$$P_\varepsilon = c_{1\varepsilon}\frac{\varepsilon}{k}P_k \tag{2.9b}$$

Production due to horizontal shear is neglected in these expressions. This is based on the assumption that horizontal length scales are large compared to the vertical length scales. Therefore it is important to discretize accurately in the vertical direction, and horizontal gradients in the production term can be neglected (Van Kester, 1994). However, these production terms are important in the situation under consideration. The effect of the horizontal shear has to be taken into account and is lumped into the horizontal eddy viscosity coefficient as will be discussed in the following section.

2.2 A depth-averaged k-ε model for determining ν_t^{2D}

2.2.1 Introduction

The 3D eddy viscosity, ν_t^v, is a scalar, which means that any directional dependency is omitted. However, this is only true in a few cases of free turbulent flows and cannot be expected to be correct as a general rule. In general the Reynolds stress in a given plane may depend on mean-velocity gradients in other planes so that the eddy viscosity is a fourth order tensor (Hinze, 1975). Owing to its complexity, this tensor is unusable in practice and therefore a scalar is mostly used in engineering practice. The recirculating flow in a harbour is highly non-isotropic and more than one turbulent length scale exists. In the mixing layer, turbulence is generated both by vertical velocity gradients (due to bottom friction) and horizontal shear, which introduces two distinct characteristic length scales. In order to account for this non-isotropic behaviour of the turbulence in this situation, a TLS turbulence model was developed.

2.2.2 Theoretical background

In the approach presented in this report, the effects of the different length-scales are accounted for separately. In contrast with the standard k-ε model, two distinct k's and ε's associated with the multiple length scales of different nature are used in order to predict the effects of the non-isotropic turbulent movements of the flow. Following (Schiestel, 1983), we can formally derive a TLS turbulence model by subdividing the TKE-spectrum into two parts as a function of the wavenumber K_1. This subdivision can be represented by decomposing the fluctuating velocity into a part due to the macro-turbulence and a part due to micro-turbulence:

$$u_i^{'} = v_i^{'} + w_i^{'}, \quad i = 1,2,3 \tag{2.10}$$

where $v_i^{'}$ represents the total amount of TKE in the area $K \leq K_1$ and $w_i^{'}$ represents the TKE for $K > K_1$. The instantaneous velocity $\mathcal{U}_i$ is decomposed in the following way

$$\mathcal{U}_i = u_i + v_i^{'} + w_i^{'} \tag{2.11}$$

where u_i is the mean velocity, consequently $\overline{\mathcal{U}_i} = u_i$, where the overbar indicates a time average. One can introduce a truncation operator by defining

$$\langle \mathcal{U}_i \rangle = u_i + v_i^{'} \tag{2.12}$$

and its complementary operator by

$$\rangle \mathcal{U}_i \langle = w_i' \tag{2.13}$$

In a similar way as done for the velocity we can define an instantaneous pressure by

$$\mathcal{P} = p + p' + \pi \tag{2.14}$$

Substituting eq. (2.11) and (2.14) into the Navier-Stokes equation

$$\frac{\partial \mathcal{U}_i}{\partial t} + \mathcal{U}_j \frac{\partial \mathcal{U}_i}{\partial x_j} = -\frac{1}{\rho}\frac{\partial \mathcal{P}}{\partial x_i} + \nu \frac{\partial^2 \mathcal{U}_i}{\partial {x_j}^2} \tag{2.15}$$

we obtain the equation for $\langle \mathcal{U}_i \rangle$:

$$\frac{\partial \langle \mathcal{U}_i \rangle}{\partial t} + \frac{\partial \langle \mathcal{U}_i \rangle \langle \mathcal{U}_j \rangle}{\partial x_j} = -\frac{1}{\rho}\frac{\partial \langle \mathcal{P} \rangle}{\partial x_i} + \beta(\mathcal{U}_i) - \frac{\partial \left\langle w_i' w_j' \right\rangle}{\partial x_j} + \nu \frac{\partial^2 \langle \mathcal{U}_i \rangle}{\partial {x_j}^2} \tag{2.16}$$

where

$$\beta(\mathcal{U}_i) = \frac{\partial \langle \mathcal{U}_i \rangle}{\partial t} - \left\langle \frac{\partial \mathcal{U}_i}{\partial t} \right\rangle \tag{2.17}$$

If K_1 is not a function of time then $\beta(\mathcal{U}_i) = 0$. The equation for $\overline{\mathcal{U}_i}$ reads:

$$\frac{\partial \overline{\mathcal{U}_i}}{\partial t} + \frac{\partial \overline{\mathcal{U}_i}\,\overline{\mathcal{U}_j}}{\partial x_j} = -\frac{1}{\rho}\frac{\partial \overline{\mathcal{P}}}{\partial x_i} + -\frac{\partial(\overline{w_i' w_j'} + \overline{v_i' v_j'})}{\partial x_j} + \nu \frac{\partial^2 \overline{\mathcal{U}_i}}{\partial {x_j}^2} \tag{2.18}$$

If we subsequently subtract eq. (2.16) from eq. (2.15), multiply by w_i' use the truncation operator and take the time average, we obtain the equation for the TKE $k^{(2)}$ in the high wave number region ($K > K_1$):

$$\begin{aligned} \frac{\mathrm{D}k^{(2)}}{\mathrm{D}t} = &- \overline{w_i' w_j'}\frac{\partial u_i}{\partial x_j} - \overline{\left\langle w_i' w_j' \right\rangle \frac{\partial v_i'}{\partial x_j}} - \overline{w_i' \beta(\mathcal{U}_i)} - \frac{\partial}{\partial x_j}\overline{(v_j' + w_j')\frac{w_i' w_i'}{2}} \\ &- \frac{1}{\rho}\frac{\partial \overline{w_i' \pi}}{\partial x_i} - \nu \overline{\frac{\partial w_i'}{\partial x_j}\frac{\partial w_i'}{\partial x_j}} + \nu \frac{\partial^2 k^{(2)}}{\partial x_j^2} \end{aligned} \tag{2.19}$$

The same procedure, using eq. (2.18) and eq. (2.16), can be applied to get the equation for v_i' and thereby the equation for $k^{(1)}$ (low wave number region):

$$\begin{aligned} \frac{\mathrm{D}k^{(1)}}{\mathrm{D}t} = &- \overline{v_i' v_j'}\frac{\partial u_i}{\partial x_j} + \overline{\left\langle w_i' w_j' \right\rangle \frac{\partial v_i'}{\partial x_j}} + \overline{v_i' \beta(\mathcal{U}_i)} - \frac{\partial}{\partial x_j}\overline{\left[(v_j' + w_j')\left(v_i' w_i' + \frac{v_i' v_i'}{2}\right)\right]} \\ &- \frac{1}{\rho}\frac{\partial \overline{v_i' p'}}{\partial x_i} - \nu \overline{\frac{\partial v_i'}{\partial x_j}\frac{\partial v_i'}{\partial x_j}} + \nu \frac{\partial^2 k^{(1)}}{\partial x_j^2} \end{aligned} \tag{2.20}$$

The first term on the right hand side of eqs. (2.19) and (2.20) is known as the production term and represents the rate at which kinetic energy is transferred from the mean flow to the turbulence and can be seen as the work done by the mean strain rate against the turbulent stresses. In the k-ε model which is implemented in TRISULA this term is modelled by means of eq. (2.9a). The fourth and fifth terms are the turbulent transport (diffusion) terms of TKE due to velocity and pressure fluctuations, respectively. Usually these terms are lumped together into one term, approximated by a gradient-diffusion expression. The sixth term is the viscous dissipation term. Based purely on dimensional arguments this term can be modelled by

$$\varepsilon \sim \frac{k^{3/2}}{\mathcal{L}} \tag{2.21}$$

where $\mathcal{L}$ is a characteristic length scale related to the turbulence. The last term is the molecular diffusion and represents the diffusion of TKE caused by the fluid's natural molecular transport process. This term is usually neglected since for large Reynolds numbers it is small compared to the turbulent diffusion term. The remaining terms, the second and the third term on the right hand side, are due to the decomposition of k into $k^{(2)}$ and $k^{(1)}$ and represent the transfer of energy from large to small scale turbulence and vice versa.

Since small eddies benefit from the loss of energy of the large eddies, the transfer term acts as a source in eq. (2.19) and a sink in eq. (2.20). The importance of this transfer is estimated by comparing the production of TKE for the small eddies, $k^{(2)}$, to the loss terms of the larger eddies. If the transfer term is small compared to the production term in the high wave number region, it can be argued that the transfer term may be neglected in the TLS turbulence model. It is noted that in the situations under consideration, i.e. in the presence of large horizontal velocity gradients, the energy supply for the large eddies is mainly determined by these velocity gradients, and therefore the transfer of energy from small to large scales is neglected a priori.

First we estimate the production of TKE for the small, 3D eddies caused by the presence of the bottom. Energy from the mean flow is transferred to turbulent movement according to

$$P_{k^{(2)}} = \tau \frac{\partial u}{\partial z} \tag{2.22}$$

where τ is the Reynolds stress per unit mass. Eq. (2.22) can be written as (using $u_* = \sqrt{c_f}u$)

$$P_{k^{(2)}} = u_*^2 \frac{\partial u}{\partial z} = c_f u^2 \frac{\partial u}{\partial z} \simeq c_f \frac{u^3}{h} \tag{2.23}$$

where h represents the water depth and c_f is a bottom friction coefficient.

Turbulence generated in the mixing layer at the harbour entrance will have a quasi-2D character. In case of strictly two-dimensional turbulence, the energy cascade process is entirely absent, which means that large turbulent structures cannot break down into small-scale turbulence by vortex stretching. In contrast with 3D turbulence, energy is transferred from small to large turbulent scales, causing the vortices to be self-organizing. At these large scales, viscous dissipation is much less effective, hence these large turbulent structures

can persist for a very long time. The only major loss of energy is due to bottom friction, generating bottom-friction induced, small-scale, turbulence. Assuming that the mean, depth averaged transverse velocity $\tilde{v}$ and the large-scale depth-averaged fluctuations $\tilde{u}'$ and $\tilde{v}'$ are much smaller than the longitudinal velocity $\tilde{u}$, the energy loss F, from which the small-scale turbulence benefits, can be estimated by (Babarutsi & Chu, 1991)

$$F_{k(1)} = \frac{c_f}{2h}\tilde{u}(2\overline{\tilde{u}'^2} + \overline{\tilde{v}'^2}) \tag{2.24}$$

where a tilde denotes a depth-averaged value. Realizing that the characteristic turbulent velocities $\tilde{u}_i'$ are at least an order of magnitude smaller that the mean velocities $\tilde{u}_i$, directly shows that this term is small compared to that in eq. (2.22), and thus can be neglected. In reality, turbulence will not be strictly 2D but rather quasi-2D which means that part of the TKE is transferred from large-scale turbulence to small scale turbulence by the vortex stretching mechanism. For very shallow water flow (almost 2D) this transfer is negligible but for more intermediate situations the transfer term may play a more important role.

In this report, the 2D characteristics of the turbulence, represented by pairing vortices generated in the mixing layer due to horizontal shear and gyres, is accounted for using a depth averaged k-ε turbulence model. In contrast with the physics of 2D-turbulence, this model is based on the energy cascade process and using this concept is thus incorrect in this situation. However, very little is known about (the modelling of) 2D turbulence in general and in complex situations including shear in particular. Therefore, despite the aforementioned objections, the k-ε turbulence model is used in this situation beyond its fundamental limits of applicability.

Using this approach, the dissipation of TKE, in the mixing layer, of the large (2D) eddies is given by

$$\varepsilon = c_D \frac{k^{3/2}}{\mathcal{L}} \tag{2.25}$$

where $c_D \simeq 0.19$ is a model coefficient. The horizontal normal Reynolds stresses per unit mass $\overline{u'^2}$ and $\overline{v'^2}$ at the centre of the mixing layer can be estimated by $(0.2\Delta u)^2$ and $(0.1\Delta u)^2$ respectively, where Δu is the velocity difference across the mixing layer (Uijttewaal & Tukker, 1997). The vertical normal Reynolds stress per unit mass $\overline{w'^2}$, is of the same order of magnitude. If we take the characteristic length scale of the 2D eddies equal to the width of the mixing layer B (for a two-dimensional free mixing layer $B \simeq 0.10\Delta x$ for $\Delta u = 0.75u$ (Brown & Roshko, 1974)), the rate of dissipation becomes

$$\varepsilon = c_D \frac{((0.2 * 0.75u)^2 + 2(0.1 * 0.75u)^2)^{3/2}}{0.1\Delta x} = 0.012\frac{u^3}{\Delta x} \tag{2.26}$$

where Δx is the longitudinal extension of the mixing layer or equivalently in this case, the width of the harbour entrance. The importance of this term depends on the ratio of the width of the harbour entrance to the local water depth. In the limiting case of two-dimensional flow, it should be equal to that given by eq. (2.24). In the situations considered in chapter 4, $\Delta x \simeq 10h$, which means that the dissipation of TKE of the large-scale turbulence, eq. (2.26), is of the

same order of magnitude as that given by eq. (2.23) and thus at least an order of magnitude larger than the bottom-friction related energy loss, eq. (2.24). However, observation of the turbulent flow reveals that large turbulent structures are long-lived (expressed by long correlation times, see next chapter), indicating that the vortex stretching (i.e. break down) of quasi-2D structures due to vertical shear in the mean-flow is of minor importance. It is therefore thought that the net energy transfer involved with vortex stretching, from large to small turbulent scales, is of minor importance compared to the production of TKE at small scales due to shear of the mean flow, as given by eq. (2.23). Since frictional forces and cascading of energy are the only two processes that diminish the energy contained in the large eddies, it is expected that the energy dissipation of the large turbulent structures is overestimated in the present turbulence model.

In the present model, the energy transfer from the depth-averaged turbulence model to the 3D turbulence model, i.e. from the large quasi-2D turbulent structures to small 3D turbulence, and vice versa has not been modelled explicitly. As shown above, under very shallow conditions the transfer term is negligible, but under more intermediate conditions, such as the situation under consideration, this will not be correct. However, modelling this transfer term is probably unfeasable for simple flows and it most certainly is for complex flows. Therefore as a first approximation these terms are neglected in the TLS turbulence model presented. The different length scales therefore are independent, although a coupling exists via the mean-flow equations.

2.2.3 Model equations

The original k-ε model as implemented in TRISULA takes only effects of turbulence due to vertical velocity gradients into account (eq. 2.9a). Turbulence generated in a mixing layer, such as the mixing layer at a harbour entrance, has to be dealt with in a different way. In TRISULA this can be done by imposing the additional "2D" eddy viscosity of eq. (2.7). However, this extra eddy viscosity has an empirical character; the value will generally vary from one situation to another. For relatively simple flow configurations it is easy to estimate the value of this coefficient, whereas for more complex transient situations, the estimation will be less trivial. Eliminating this aspect is one of the major advantages of the turbulence model proposed.

The TLS turbulence model exists of two separate single-length-scale turbulence models, that account for the different length scales present in the flow. The small-scale turbulence generated by bottom friction (and other vertical velocity gradients) is modelled by the 3D k-ε model of section 2.1 whereas the effects of the larger eddies generated in the mixing layer are embodied in a depth-averaged k-ε model. The models represent the 3D- and 2D eddy viscosities of eq. (2.7), respectively.

The equations used for the depth-averaged TKE and dissipation of TKEare (Booij, 1989), (Rodi, 1980),

$$\frac{\mathrm{D}\overline{k}}{\mathrm{D}t} = \frac{\partial}{\partial x}\left(\frac{\nu_t}{\sigma_k}\frac{\partial \overline{k}}{\partial x}\right) + \frac{\partial}{\partial y}\left(\frac{\nu_t}{\sigma_k}\frac{\partial \overline{k}}{\partial y}\right) + \overline{P}_k - \overline{\varepsilon} \qquad (2.27a)$$

$$\frac{\mathrm{D}\overline{\varepsilon}}{\mathrm{D}t} = \frac{\partial}{\partial x}\left(\frac{\nu_t}{\sigma_\varepsilon}\frac{\partial \overline{\varepsilon}}{\partial x}\right) + \frac{\partial}{\partial y}\left(\frac{\nu_t}{\sigma_\varepsilon}\frac{\partial \overline{\varepsilon}}{\partial y}\right) + \overline{P}_\varepsilon - c_{2\varepsilon}\frac{\overline{\varepsilon}^2}{\overline{k}} \tag{2.27b}$$

where the overbar now indicates depth averaging. The production terms, $\overline{P}_k$ and $\overline{P}_\varepsilon$, are determined by the horizontal shear only.

$$\overline{P}_k = \overline{\nu}_h \left[\left(\left(\frac{\partial \overline{u}}{\partial y}\right) + \left(\frac{\partial \overline{v}}{\partial x}\right)\right)^2 + 2\left(\frac{\partial \overline{u}}{\partial x}\right)^2 + 2\left(\frac{\partial \overline{v}}{\partial y}\right)^2\right] \tag{2.28a}$$

$$\overline{P}_\varepsilon = c_{1\varepsilon}\frac{\overline{\varepsilon}}{\overline{k}}\overline{P}_k \tag{2.28b}$$

It is presumed that if all velocity gradients would be included in eq. (2.9a) and eq. (2.28a), turbulent intensities would be overestimated.

In order to get a well-posed problem, boundary conditions for both the k and ε equations in both turbulence models have to be specified. At closed boundaries, often the so-called law of the wall is used. In this region advection, pressure gradient and molecular diffusion can be neglected, yielding a constant Reynolds shear stress. In this log-layer, where production of TKE equals the dissipation of TKE, k and ε read

$$k = \frac{u_*^2}{\sqrt{c_\mu}} \tag{2.29a}$$

$$\varepsilon = \frac{u_*^3}{\kappa y} \tag{2.29b}$$

where u_* is the friction velocity and y a coordinate normal to the wall. These expressions are valid for a fully developed flow in the region $30 < y^+ < 130$ where $y^+ = y\frac{u_*}{\nu}$ is a dimensionless coordinate. Estimating u_* by $\frac{\overline{u}}{15}$ and choosing $\overline{u} = 1$ m/s as a typical mean flow velocity, the constant stress layer will extend about 2 mm from the wall. In most numerical calculations, the first grid cell will be much larger than this value, hence the law of the wall is formally used beyond its region of validity.

At the inflow boundary of the 3D turbulence model, the TKE must be specified. A logarithmic velocity profile and a linear distribution of k is assumed, on the basis of the shear stress at the bed (Delft Hydraulics, 1994)

$$k = \frac{u_{*b}^2}{\sqrt{c_\mu}}\left(1 - \frac{z}{d}\right) \tag{2.30}$$

For the ε boundary condition, a hyperbolic distribution is assumed, again on the basis of the shear stresses at the bed (Delft Hydraulics, 1994)

$$\varepsilon = \frac{|u_{*b}|^3}{\kappa z} \tag{2.31}$$

In these equations u_* is a friction velocity (where subscript b refers to the bottom) and κ is the Von Kármán constant. Boundary conditions at the inflow boundary for the depth-averaged

turbulence model are taken equal to the depth-averaged values of the 3D turbulence model. The inflow boundary conditions for k and ε are of minor importance since most of the TKE is generated inside the domain of computation. At the outflow boundary, symmetry boundary conditions are imposed. Such conditions are also imposed at the free surface in case of the 3D turbulence model.

2.2.4 Numerical aspects

The TRISULA version used for the computation solves the momentum equations using an ADI time integration method (Delft Hydraulics, 1994). The finite difference schemes for spatial integration are defined on a staggered grid. In contrast with the original TRISULA definition, k and ε were shifted from the water elevation points to the water depth points, see Figure 2.1. The advantages of this displacement are twofold. First of all, the Reynolds shear stresses are computed more accurately since less averaging is needed. Averaging in computing normal Reynolds stresses increases, but these terms are of minor importance. Besides this, implementation of the Dirichlet boundary conditions eq. (2.29a) and (2.29b) for rigid walls is straightforward since depth points of the staggered grid are defined on the computational boundaries.

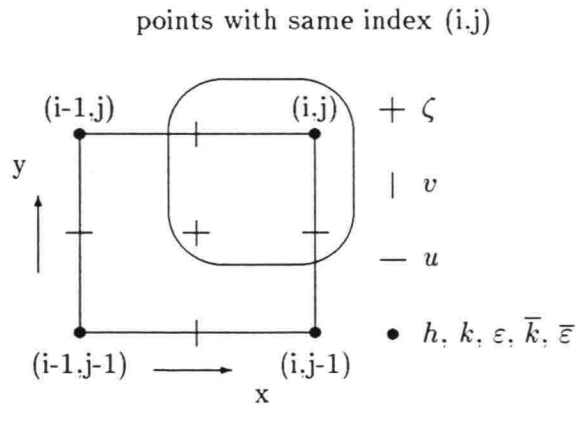

Figure 2.1: Definition of staggered grid

In order to increase computational efficiency, an explicit first-order upwind scheme is used for the discretization of the advective terms of the momentum equation and the turbulence models. The advective terms are discretized with a first order upwind method that ensures positive solutions (no wiggles) which is imperative when solving the k and ε transport equations. However, this method suffers from cross-wind diffusion when the local velocity vector is not aligned with the grid. This numerical diffusion may cause a large error in the solution, as will be shown in chapter 4. Grid refinement or grid adaptation to make the grid aligned with the streamlines are expensive remedies to suppress this disadvantage. Another method, which is applied herein for the advective terms, is to employ the upwind scheme along streamlines rather than grid lines. Depending on the local velocity vector (or more precisely, the local CFL-number) in the depth point, three different points on the grid

are involved in computing the advection. If for example we consider the situation where $u > v > 0$ and $\mathrm{CFL}_x > \mathrm{CFL}_y$ the points with index (i.j), (i-1.j) and (i-1.j-1) are used whereas in the conventional first order upwind method points with index (i.j), (i-1.j) and (i.j-1) are employed (Vreugdenhil & Koren, 1993). This way a more accurate and positive solution is guaranteed. The artificial cross-wind diffusion related to first-order differencing smears out the solution in regions where the flow crosses the cells under a considerable angle, causing the turbulence to die out rapidly. Application of the integration along streamlines suppresses this numerical side-effect yielding a physically more realistic solution. This result supports the opposition against usage of standard first-order upwind for advective modeling in multi-dimensional calculations, e.g. (Leonard & Drummond, 1995). Diffusion terms are discretized using second-order central differences.

In accordance with the 3D turbulence model, $\overline{k}$ and $\overline{\varepsilon}$ are discretized in a non-conservative way. It is plausible that this will hardly damage the results for the 3D model since production and dissipation of k will dominate the solution of these equations in the entire computational region. In case of the depth averaged turbulence model, this is less likely to be correct: turbulence generated in the mixing layer will be transported into the harbour where it slowly decays (Booij, 1991). However, due to the selected position of $\overline{k}$ and $\overline{\varepsilon}$ on the staggered grid, it is not possible to use a conservative form. Possible implications of this aspect for the computed solution are discussed in chapter 4.

Chapter 3

Laboratory measurements

In this chapter, laboratory measurements, carried out in April 1997 at the Hydromechanics Laboratory of the Civil Engineering Faculty of Delft University of Technology, are presented. The aim of these experiments was to determine flow characteristics of a stationary recirculating flow in a harbour. Mean flow quantities as well as the turbulent fluctuations were measured. Results of the measurements are used for model validation in chapter 4. Although there is no stratification, which in general enhances the three-dimensional character of the flow, three-dimensionality is an important property of the flow. Therefore measurements were also carried out at several vertical positions at a fixed coordinate in a horizontal plane.

Two different geometries are considered; the first situation studied is a scale model of yacht harbour "'t Steel" on the river Meuse between kilometer 78.4 and 78.9 (scale 1:50 in both vertical and horizontal planes). In a previous study, several measures to reduce the siltation of the harbour were investigated, one of which resulted in a sill placed in the harbour entrance (Van Schijndel, 1997). This situation was the basis of the second series of measurements. Results of these measurements are available on cd-rom, which contains documented files of unprocessed data.

3.1 Experimental set up

3.1.1 Scale model of yacht harbour "'t Steel"

The physical scale model was based on an existing model used for investigation of reduction of harbour siltation (Van Schijndel, 1997). Some modifications were made to the model. First of all, the sudden widening of the river, upstream of the harbour entrance, was eliminated in order to suppress locally generated turbulence. Hereby, turbulence measured at the harbour entrance originates mainly from the mixing layer and is not influenced by turbulence generated upstream. This way it is easier to draw conclusions about the performance of the different turbulence models at regions of interest. Besides, the physical domain was diminished in order to reduce computational costs, without influencing the main properties of the flow. An overview of the final scale model is given in Figure 3.1.

At the inflow boundary a flow rate of 0.041 m^3/s was imposed. This yields a Reynolds number, $R\epsilon = \frac{uh}{\nu}$, based upon the mean flow velocity in the river, u, and the mean water

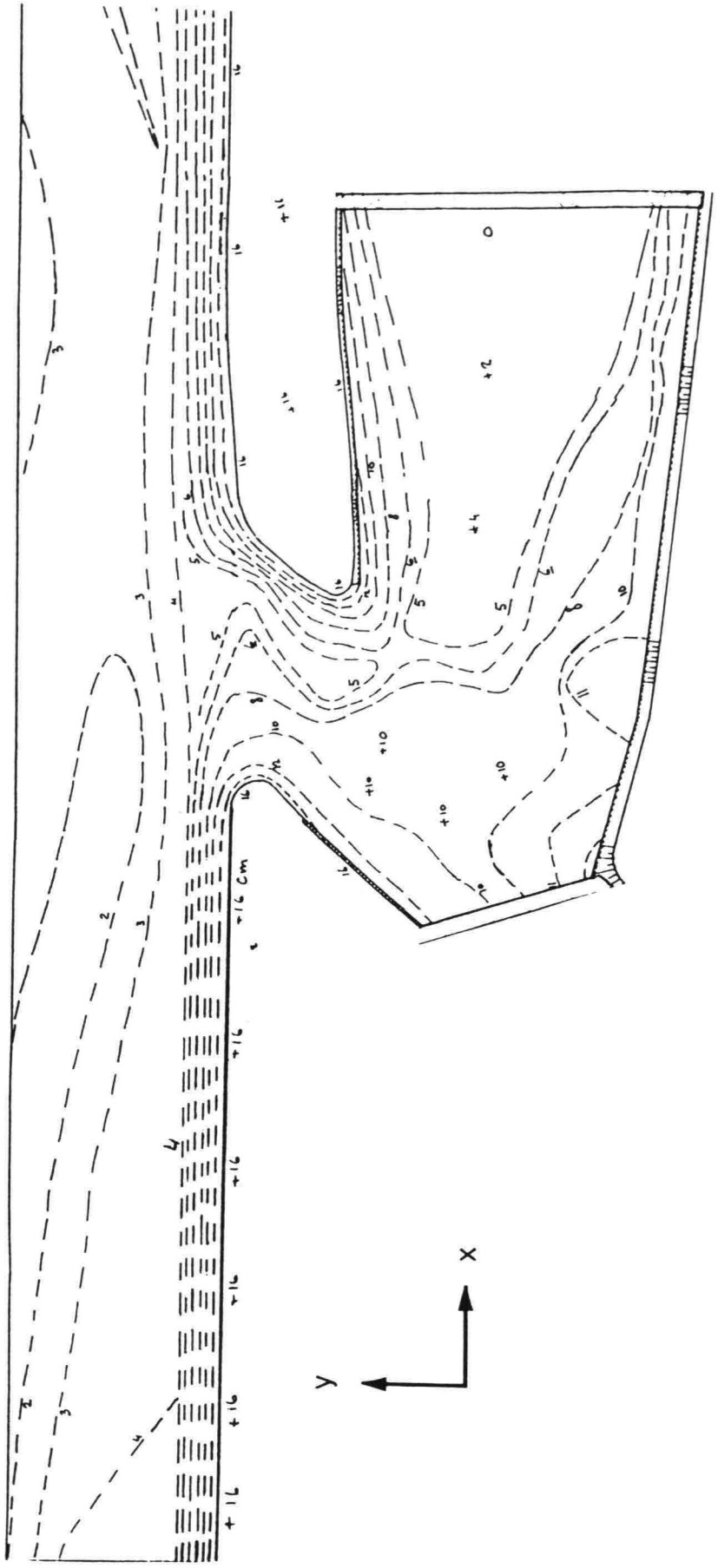

Figure 3.1: Adapted physical scale model of yacht harbour "'t Steel". Bottom heights in cm above datum level.

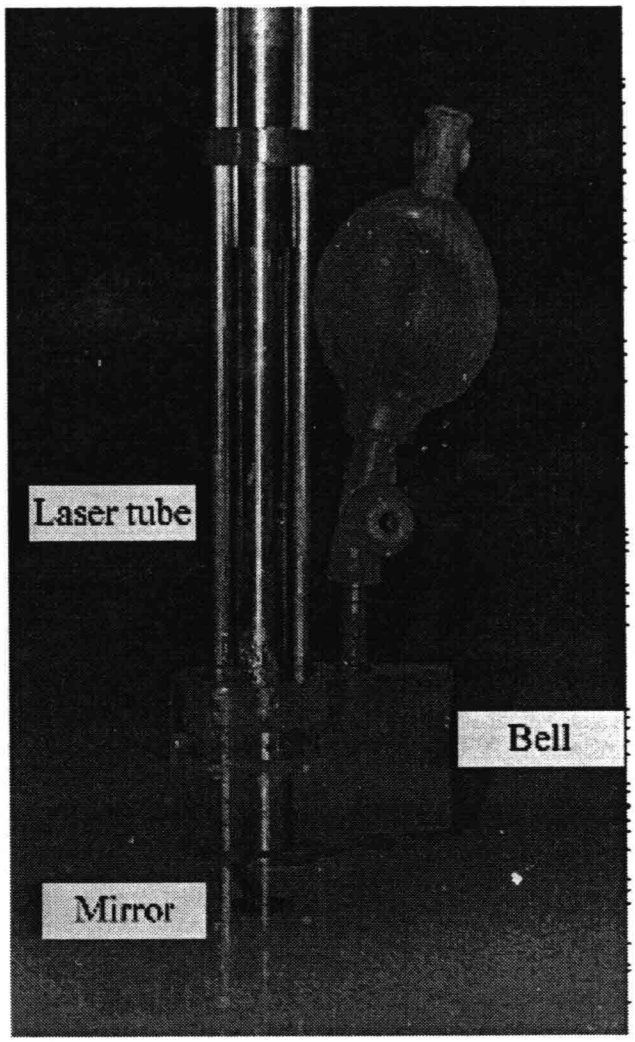

Figure 3.2: Laser Doppler anemometer HILDA with bell attached to it

depth in the river, h, of approximately 40000 which means that the flow is turbulent. The Froude number, $Fr = \frac{U}{\sqrt{gL}}$, equals 0.28 which satisfies the conditions that the flow should be sub-critical and that no surface waves are generated. In order to prevent large eddies, with a characteristic horizontal size of the river width, from entering the model, guiding walls were placed at the inflow boundary. The outflow boundary consisted of a short-crested weir, eliminating downstream influences.

3.1.2 Measuring equipment

The measurements were carried out using the so-called HILDA, a submersible laser Doppler anemometer (LDA) of Delft Hydraulics, see Figure 3.2. The laser beams, radiated by the vertical laser tube are reflected by an opposing mirror and received by two glass fibers. The

measuring volume is situated half-way between the tube and mirror, which poses a restriction to the vertical distance over which velocities can be measured. The maximum water depth in the region of interest is about 10 cm and consequently a significant part of the water depth would be excluded from the measurements. A further restriction was imposed by the position of the receiving glass fibers, which are situated well above the laser tube. In order to let the apparatus work properly, these fibers must be positioned underwater and thus the effective distance over which velocities can be measured is further reduced. To overcome this drawback, a small bell filled with water by creating under-pressure, was attached to the laser tube. By comparing LDA-measurements with and without the bell at the same position, it was concluded that the disturbing effect of the bell can be neglected as long as it penetrates the water column only a few mm's. Therefore the bell was shifted upward for measurements deeper in the water column.

The LDA measures velocities in a horizontal plane in two orthogonal directions simultaneously, which makes it possible to determine horizontal Reynolds stresses. However, vertical velocities are not measured, leaving the vertical Reynolds stresses and the exact total turbulent kinetic energy, $k = \frac{1}{2}(\overline{u'^2} + \overline{v'^2} + \overline{w'^2})$, undetermined.

The sampling rate of the LDA measurements and the sampling period are determined by the accuracy required and by the information we want to obtain from the measurements. Using the second order statistical moment, defined by

$$\overline{(u_i')^2} = \frac{1}{N}\sum_{n=1}^{N}(u_n')^2 \tag{3.1}$$

we can estimate the error for the normal Reynolds stresses measured or the TKE. Approximating the turbulent velocity fluctuations by a Gaussian or normal distribution function, which is correct in many situations, the statistical error ϵ in estimating the normal Reynolds stresses or TKE becomes (Tukker, 1997)

$$\epsilon = \sqrt{\frac{2}{M}} \tag{3.2}$$

where M is the number of independent measurements. If we accept a relative error of 10 % this requires a number of independent measurements equal to 200. The measuring time depends on M and the time-scales of structures present in the flow. A suitable measure for the maximum time interval during which a three-dimensional turbulent velocity is correlated with itself, and thus represents a characteristic time scale of the large turbulent scales, is the integral time scale $\mathcal{T}$ defined as (Tennekes & Lumley, 1972)

$$\mathcal{T} \equiv \int_0^\infty \rho(\tau)d\tau \tag{3.3}$$

where τ is a time shift and $\rho(\tau)$ is the autocorrelation function defined by

$$\rho(\tau) \equiv \frac{\overline{u_i'(t)u_i'(t+\tau)}}{\overline{u_i'(t)^2}} \tag{3.4}$$

where t is the real time. The ratio of the measuring time and twice the integral time scale, $\frac{T_m}{2\mathcal{T}}$, may be regarded as the number of independent samples M in a record of length T_m (Tennekes & Lumley, 1972). However, in quasi-2D shear flows with 2D structures, such as the shallow water mixing layer in the harbour entrance, for example, these structures show a quasi periodic behaviour (Uijttewaal & Tukker, 1997) and (Tukker, 1997). The large-scale quasi-periodic structures are responsible for large correlation coefficients of varying sign for large time-shifts τ. This makes the definition of M using the time scale $\mathcal{T}$ unusable in these situations. Therefore, it is more practical to consider M equal to the number of periods of the quasi-periodic fluctuations present in the measured time signal, as suggested in (Tukker, 1997). Since there is no a priori information of the flow, the integral time scale is estimated by

$$\mathcal{T} = \frac{\mathcal{L}}{U} \tag{3.5}$$

The characteristic turbulent length scale $\mathcal{L}$ of the 3D turbulence, is restricted by the water depth of the model. However, 2D-dimensional structures up to several times the water depth can exist. For a shallow water mixing layer, that develops in the harbour entrance of the model, structures with a size three times the mixing layer width can exist (Tukker, 1997). The width of the mixing layer is estimated by the linear growth of a two-dimensional mixing layer (i.e. for infinite depth) (Brown & Roshko, 1974)

$$\frac{\Delta B}{\Delta x} = 0.18 * \frac{(u_r - u_h)}{(u_r + u_h)} = 0.18 * \lambda \tag{3.6}$$

where $u_r - u_h$ is the velocity difference over the mixing layer and B is the mixing-layer width defined by the velocity profile maximum slope thickness

$$B = \frac{u_r - u_h}{\left(\frac{\partial u}{\partial y}\right)_{max}} \tag{3.7}$$

As a first guess, the velocity of the gyre u_h will be about $0.25u_r$ (Booij, 1986), where u_r is the mean flow velocity in the river, yielding a broadening of the mixing layer equal to $0.1\Delta x$. The maximum expected layer width will therefore be about 10 cm, yielding largest eddies with a size of about 30 cm. If we approximate the advective velocity of the eddies to be equal to half the river velocity (taking the advective velocity equal to the velocity in the centre of the mixing), this leads to a integral time scale of about 2 s and a measuring time of 7 minutes. In the experiments a measuring time of 10 minutes was used.

In order to analyze the spectral distribution of the turbulence down to the viscous sub-range, the dimensionless wave number $\mathcal{L}k_{max}$ should be at least 100 (Nezu & Nakagawa, 1993). Since the macro-(or integral) scale of the 3D turbulence scales with the flow depth h, the maximum response frequency can be estimated as follows

$$f_{max} = \frac{k_{max}u}{2\pi} \geq \frac{100u}{2\pi\mathcal{L}} \simeq \frac{50u}{\pi h} \tag{3.8}$$

Accounting for aliasing and taking $u = 0.3$ m/s and $h = 0.1$ m leads to a frequency of 100 Hz.

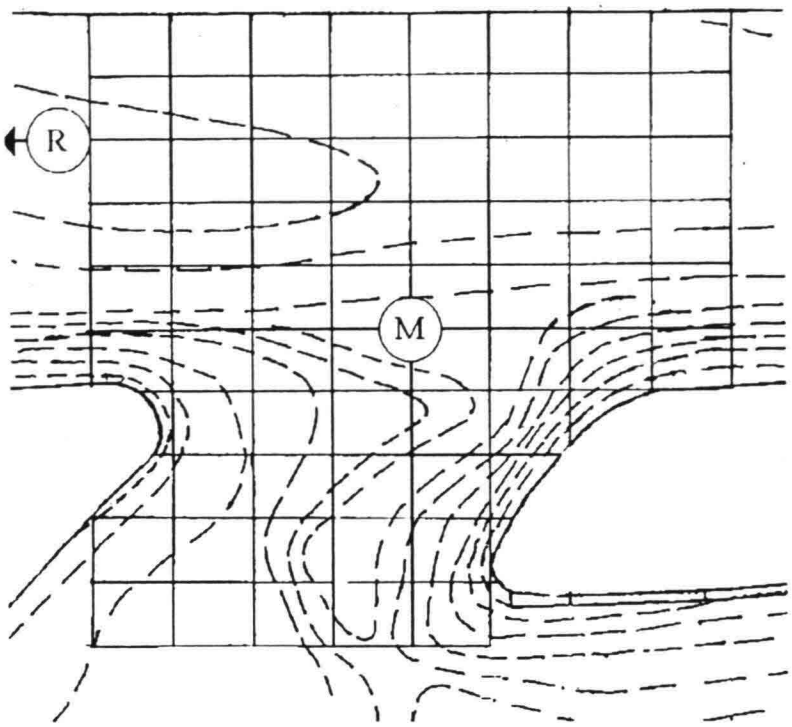

Figure 3.3: Measuring grid. Letters R and M indicate positions in river and mixing layer, respectively

3.2 Results of measurements

Four series of measurements were carried out for the two different flow configurations. Two series concern the measurements without the bell attached to the LDA for both the situation without and with a sill in the harbour entrance. In the concluding two series the bell was attached to the LDA.

An overview of the measuring grid is shown in Figure 3.3. The grid spacing in the main flow direction of the river equals 25 cm while in the direction perpendicular to the mean flow the spacing is 20 cm. Some extra measuring positions were added near the sill and in the mixing layer between the river and harbour in order to obtain more information at these specific places. In the harbour-area only some reference measurements were carried out: in these (shallow) areas, where the flow is almost 2D, velocities are mainly determined by using a particle tracking system (Van Noort, 1997). Upstream of the harbour entrance some measurements for verifying the boundary conditions imposed in the numerical model were carried out. These locations are not visualized in Figure 3.3. An exact overview of the sample positions can be found in the "info.txt" file on the earlier mentioned cd-rom.

mean-velocities

One of the main objectives of the laboratory measurements, was to obtain mean velocities for numerical model validation. In the region where the flow has a three-dimensional character, i.e. at the harbour entrance, mean velocities were obtained from LDA-measurements. From these data, the mean velocity was computed by

$$u_i = \frac{1}{N}\sum_{n=1}^{N} \mathcal{U}_i^n \tag{3.9}$$

where $\mathcal{U}_i^n$ is the instantaneous velocity in the i-direction and N is the number of samples. In regions where the flow is nearly two-dimensional, such as the harbour area, velocities can be determined by particle tracking velocimetry (PTV). With this technique, small floating particles that are released in the water, are monitored by a camera. Afterwards, these video images are analyzed by a computer program yielding a dense vector field. This information is only available for the situation without a sill in the harbour entrance. In addition, quantitative information about the velocities in the quasi-2D region, approximate streamlines at the water surface can be obtained from these vector field, which is useful for judging the computational results in a more qualitative manner. Moreover, streamlines at the bottom were revealed by means of $KMnO_4$ particles. The results of the LDA and PTVmeasurements are discussed in the next chapter together with the computational results.

velocity correlations

In order to gain insight in the spatial dimensions of the turbulent structures that develop in the mixing layer, velocity correlations are used. One can directly estimate the characteristic turbulent length scales by considering the spatial correlation between the same fluctuating quantity at a certain time. However, measuring these spatial correlations is a laborious task and therefore time- or autocorrelations are used for determining typical length scales by multiplying the characteristic time-scale by the mean local velocity. This method can only be applied when the average life time of an eddy is large compared to the mean transport time needed to detect it, a requirement which in general this is fulfilled: we can approximate the rate of change, consisting of the material derivative and an advective part, by

$$\frac{\partial}{\partial t} \sim \frac{u'}{\mathcal{L}} - \frac{u}{\mathcal{L}} = \frac{u}{\mathcal{L}}(1 - \frac{u'}{u}) \tag{3.10}$$

where the characteristic time scale of an eddy is equal to $\mathcal{L}/u'$. The ratio u'/u is a measure for the turbulence intensity and is small in most flows. This means that the eddy hardly changes while it is advected along the measuring probe, i.e. the turbulence is "frozen" (Taylor hypothesis). In case of 3D turbulence we can use expression 3.3 as a definition of the integral time scale whereas in case of 2D turbulence this time scale can be estimated by the periodic behaviour of the correlation function, as discussed in section 3.1.2. The spatial extension of the turbulent structures is revealed most clearly by considering the transverse velocity component, i.e. the velocity in horizontal direction perpendicular to the mean flow. In Figure 3.4, the

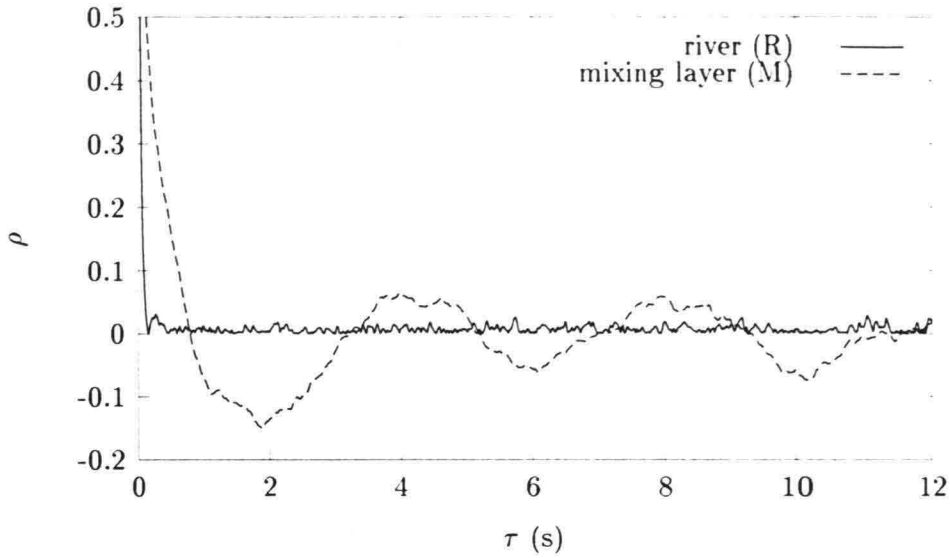

Figure 3.4: Autocorrelationfunction of the transverse velocity fluctuations (v') in the river (R) and mixing layer (M); location R and M are shown in Figure 3.3.

autocorrelationfunctions of the transverse velocity fluctuations in the river and mixing layer are shown. The positions are indicated by the letters R and M in Figure 3.3, respectively. The exact position of R is located 50 cm upstream of the position indicated, equal to two grid spacings in the mean flow direction. In the vertical direction, the sample points are positioned somewhat below mid depth.

In the river, the fluctuating velocities are shown to be correlated for a small time-shift τ, indicating that only small-scale turbulence is present at this position. The spatial dimension of the small-scale turbulence is determined by multiplying the integral time scale, which is about 0.15 s, with the mean velocity at this position. This yields a turbulent length scale of 9 cm, which is of the order of the water depth. This small scale turbulence can also be recognized in the autocorrelation function in the mixing layer; near the origin, the autocorrelationfunction drops suddenly from 1 to about 0.3 (where the slope diminishes) indicating limited coherence of the small scale motions. The existence of large coherent turbulent structures can easily be discerned from Figure 3.4. The slowly decaying autocorrelation indicates a spatial dimension of the large structures of about .9 m, which is much larger than the local water depth. The spatial extension of the turbulent structures seems to be larger than the estimated size of the eddies by eq. (3.6), which is due to the stretching of the eddies in the longitudinal direction. The existence of these large structures was visualized during the experiments by injecting upstream of the mixing layer, dissolved $KMnO_4$ into the water, see Figure 3.5.

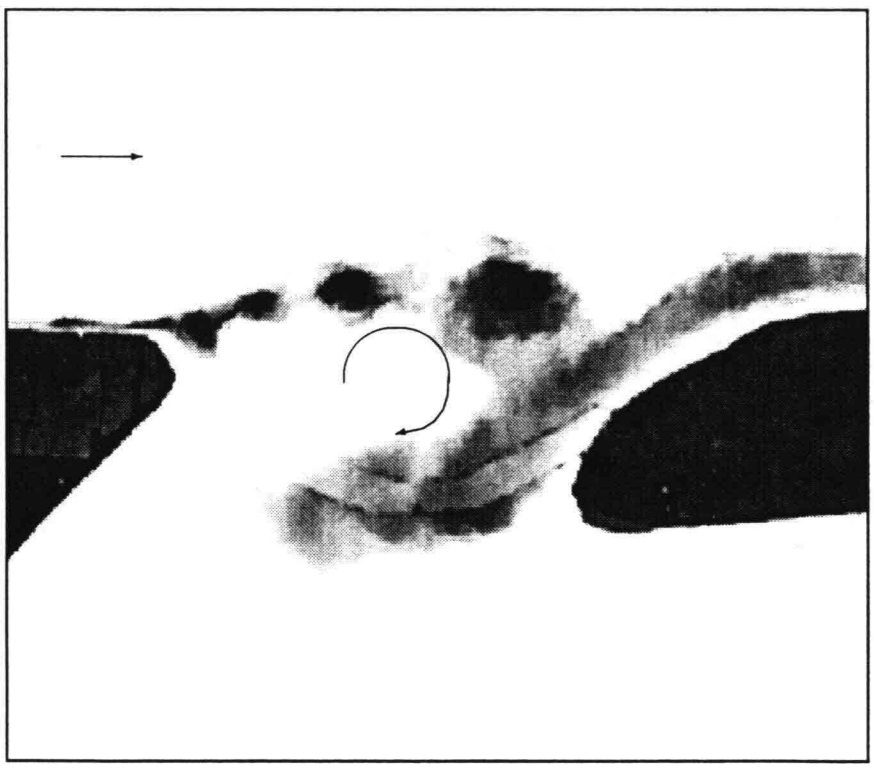

Figure 3.5: Top view of the shallow-water mixing layer and the approximate flow pattern. Four (developing) quasi 2D structures and a gyre can be discerned. The width of the harbour entrance is approximately 10 times the average water depth.

one-dimensional power spectra

The TLS turbulence model described in chapter 2. was developed for (quasi-) 2D turbulent flow. Therefore, data used for validation of the model should concern this type of flow. The two-dimensional character of the turbulence of the mixing layer due to the shallowness of the flow, is most easily illustrated by considering the one-dimensional power-density spectrum of the turbulence, although it can also be studied by means of correlation in the vertical direction (Uijttewaal & Tukker, 1997). The data set was split up into 40 overlapping intervals. of which a power spectrum was computed by fast fourier transform. After that. the results were averaged in order to obtain a smoothed curve.

Transverse velocity fluctuations were used for the computation of characteristic power spectra, the results of which are shown in Figure 3.6. The same sample positions as for the autocorrelation function were used for the power spectra. At low frequencies. the energy can be seen not to go to zero, which is due to the effect of aliasing (Tennekes & Lumley. 1972). Apart from the difference in total amount of turbulent energy, the major difference between the two spectra occurs at low frequencies. A peak at low frequencies near 0.3 Hz (which is similar to a characteristic period of 3.3 s) occurs in the energy spectrum of the sample point in the mixing layer, which can be ascribed to quasi two-dimensional turbulent structures: the upcascading of energy from small to large eddies, related to the 2D turbulence. leads to large well-organized structures which is reflected by this peak. The -3 slope of the spectrum in this region is in agreement with the development of quasi-two-dimensional turbulence and the related inverse energy cascade (Kraichnan, 1967), (Lesieur, 1990).

At higher frequencies a -5/3 slope can be discerned, which is related to an inertial subrange in three-dimensional turbulence. This reflects the presence of an energy cascade related to the vortex stretching process. The range in which the slope equals -5/3 is rather small due to the relatively low Reynolds number, indicating a small separation between the macro- and micro-structure of the turbulence.

Reynolds stresses

During the LDA experiments, the instantaneous velocities U and V were measured simultaneously, which enables us to determine horizontal Reynolds stresses. These Reynolds stresses, and the Reynolds shear stresses in particular, account for the transfer of momentum across the mixing layer and are the driving forces responsible for the development of the gyres in the harbour entrance and the harbour itself. The correct representation of the Reynolds stresses is therefore an important criterion to judge the turbulence model by. The Reynolds stress per unit mass $\overline{u'v'}$ is determined from the measurements by:

$$\overline{u'v'} = \frac{1}{N}\sum_{n=1}^{N} u_n' v_n' \tag{3.11}$$

In the next chapter, experimental results are discussed together with the computed ones.

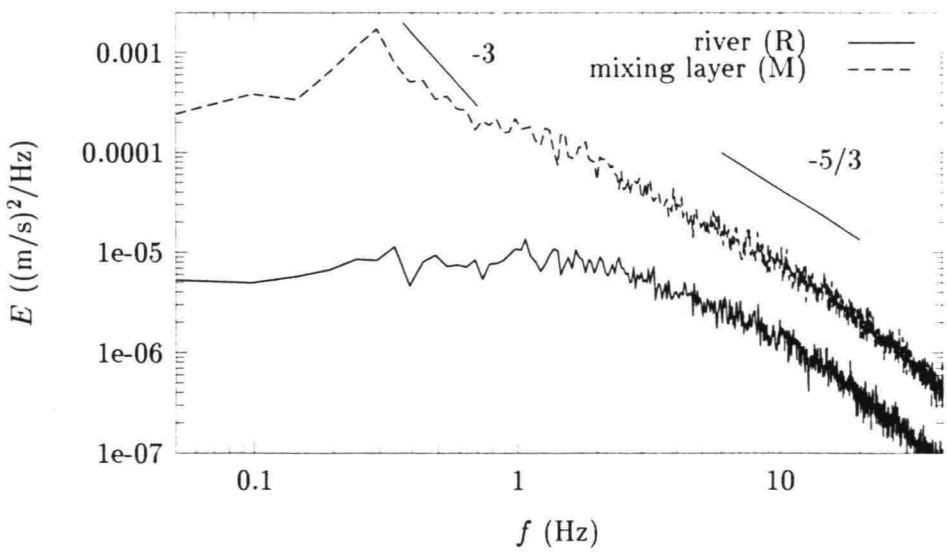

Figure 3.6: One-dimensional power-density spectrum of transverse velocity fluctuations (v') in the river and mixing layer

Chapter 4

Modelling recirculating harbour flow

In this chapter results of numerical computations are discussed and compared with experimental results. Two different geometric configurations were studied. The first concerns a cavity driven flow in a square model harbour. Measurements of mean velocities carried out by (Langendoen, 1992) are used for model verification. After that, results from modelling the more complex harbour flow, discussed in the previous chapter, are compared to measurements. The figures showing the results can be found in the appendix "figures".

4.1 Cavity driven flow in a square model harbour

4.1.1 Model description

The first situation to be considered is that of a square harbour, 1×1 m^2, that is situated on a 18 m long and 1 m wide prismatic channel. The depth is uniform throughout the entire model and equals 0.11 m and sidewalls of the model are vertical. At the inflow boundary a flow rate of 0.042 m^3/s is imposed yielding a mean flow velocity of 0.37 m/s. At the harbour entrance a mixing layer will develop due to the velocity difference between the river and harbour. Momentum is transferred by turbulence from the river to the harbour, resulting in a recirculating flow (gyre) which covers the whole harbour.

At four different levels, 0.015 m, 0.04 m, 0.06 m and 0.08 m above the bottom, mean velocities haven been measured at various positions in a horizontal plane. Besides, more detailed information on the vertical distribution of the horizontal velocity components is available at one position P near the stagnation point, see Figure 4.1. For a hydraulically rough bottom the measured value of the bed-friction coefficient is equivalent with a roughness height according to Nikuradse, k_N, equal to $4.05 \text{x} 10^{-3}$ m. These data are used for model verification. For more detailed information on the experiments, the reader is referred to (Langendoen, 1992).

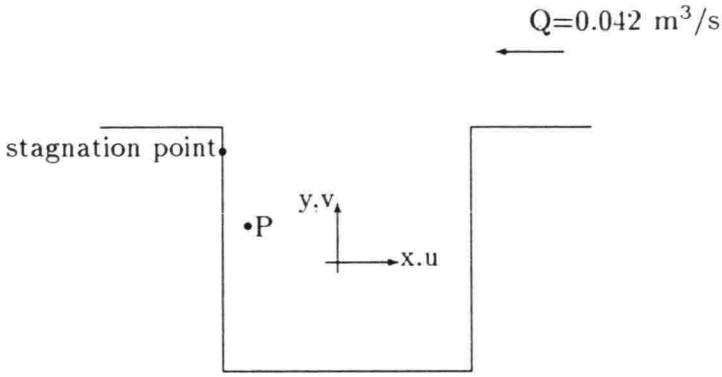

Figure 4.1: Definition sketch of square harbour

4.1.2 Results

The harbour and a section of the river with a length of 5 m were schematized. The open boundaries were situated at 2.5 m from the centre-line of the harbour. At the inflow boundary the flow rate equal to the flow rate in the physical model was imposed and the vertical velocity profiles were logarithmic.

Computations were carried out on different grids to check the convergence of the solutions. The converged solution was obtained on a grid consisting of 88 x 64 grid points. The grid spacing in the harbour varies between 2 cm near the closed boundaries and mixing layer and 4.3 cm at the centre of the harbour see Figure F.1. In the vertical direction 10 layers were used, with decreasing vertical spacing towards the bottom (15, 15, 14, 14, 12, 10, 8, 6, 4 and 2 per cent of the water depth) in order to represent large gradients near the bottom accurately. Only results from the converged solution, i.e. on the dense grid, are presented in this section.

In order to judge the computed results, two graphical presentations of velocities are used. At four different levels above the bottom, velocities along two transects through the centre of the gyre are available. Besides, vertical velocity profiles of both horizontal velocity components at position P near the stagnation point are available for comparison, see Figure 4.1. First of all, velocities resulting from applying all three turbulence models under consideration, i.e. the standard 3D k-ε model, the k-ε model as implemented in TRISULA and the new TLS turbulence model, are compared at four different levels. To obtain the standard 3D k-ε model, horizontal derivatives were included in the production term of eq. (2.9a):

$$P_k = \nu_t^v \left(\frac{\partial u_i}{\partial x_j} + \frac{\partial u_j}{\partial x_i} \right) \frac{\partial u_i}{\partial x_j} \tag{4.1}$$

No 2D eddy viscosity ν_t^{2D}, either constant or calculated from the depth-averaged turbulence model, was added to the eddy viscosity thus calculated. An additional 2D-eddy viscosity was added to the turbulence model implemented in TRISULA as discussed in chapter 2. In an earlier paper this 2D-viscosity was taken equal to $5\text{x}10^{-4}$ m^2/s, which value was based upon the turbulence generated in the mixing layer (Langendoen & Kranenburg, 1993). The measured and computed velocities at 0.015 m, 0.04 m, 0.06 m and 0.08 m above the bottom are compared along two transects through the measured centre of the gyre, see Figure F.2.

In the x-direction the u-component of the velocity vector is plotted and in y-direction the v-component. Linear interpolation was used to obtain computed velocities at these heights. It can be concluded from this figure that all models perform equally well at these positions and agree well with the measured data, including the computed centre of the gyre. It must be noted that the success of the TRISULA model can be ascribed to the correctness of the constant eddy viscosity; two-dimensional calculations of the flow in a square harbour (Booij, 1989) with a depth-averaged k-ε model, confirm that the eddy viscosity is almost constant in the harbour. In practical more complex situations where the eddy viscosity varies in time and space, this approach is likely to fail.

A major difference between the computed width of the mixing layer for the standard k-ε turbulence model and the TLS turbulence model is observed. Defining the mixing layer width by eq. (3.7), the linear growth of the mixing layer in case of the standard k-ε model equals $B = .13x$, where x is the coordinate in the mean flow direction of the river and has its origin at the seperation point. The TLS model, on the other hand, yields a larger growth of the mixing layer that is approximately equal to $B = .20x$. The data from (Langendoen, 1992) are too coarse to draw any definite conclusion about the growth of the mixing layer in the harbour entrance. However, more detailed measurements of velocities at mid-depth in a 1x1 m^2 square harbour with similar flow conditions ($h = 0.105$ m and $\lambda \simeq 0.8$ where λ is defined as in eq. 3.6) are available from (Booij, 1986). Booij measured a width of the mixing layer of about $b = 0.17x$ where b is the distance between the points where the velocity in the mixing layer differs a factor $(u_r - u_h)/2\epsilon$ from u_r and u_h. Assuming that the velocity distribution in the mixing layer is an error integral, the distance b is related to B as $B = 1.39b$, hence $B = 0.23x$. Note that the growth of the mixing layer between the river and harbour is significantly larger than observed by (Brown & Roshko, 1974) and (Tukker, 1997) for free mixing layers. It can be concluded that the proposed TLS turbulence model performs better than the standard k-ε model in the mixing layer region, something that will be supported later in this report.

Figure F.3 shows the distributions of the horizontal velocity components in the vertical at point P, 0.4 m from the transition from harbour to river and 0.1 m from the harbour sidewall. Comparing computed distributions with the measured ones, it is observed that the characteristic bulb appearing near the bottom of the velocity profile in the y-direction, i.e. v, (which results from the aforementioned flow of high-momentum fluid in the mixing layer from close to the surface towards the bottom in the harbour) is predicted better with the TLS models than with the standard model, both qualitatively and quantitatively. Especially near the surface, where the eddy viscosity vanishes in case of the standard turbulence model, better agreement with measurements is found. It must be noted that the existence of the bulb in the computed profile was found to be strongly dependent upon the turbulence model used; several other turbulence models yielded, in contrast with the measurements, log-like velocity distributions and thus failed to represent this 3D feature of the flow at all.

The abovementioned conclusions also hold for the secondary motion normal to the wall (which is caused by the recirculating flow in the harbour) although the magnitude of this current is underpredicted considerably with all turbulence models. It is clear that in contrast with the TLS model the standard turbulence model is not capable of predicting the typical shape of the velocity profiles in primary and secondary flow directions.

The boundary conditions imposed at the walls for k and ε may play an important role in predicting the abovementioned bulb and the secondary flow. Near the stagnation point, these boundary conditions are likely to be incorrect since they were derived for a developed flow, which obviously is not present in that area. The wall-friction eliminates part of the pressure build-up near the wall, so that the secondary current is reduced. Besides this, the flow near the stagnation point does not fulfill the restrictions following from the assumed hydrostatic pressure distribution, i.e. the flow is locally non-hydrostatic. The influence of vertical accelerations near the solid boundary are not "felt" at monitoring position P, which influences the velocity profile of the secondary current significantly. As a consequence, vertical velocities are concentrated near the sidewall introducing high velocities and velocity gradients.

In order to get a better picture of the flow pattern within the harbour, vector plots of the 10 computational layers are shown in Figure F.4. Notice that there are several stagnation points, the positions of which can all be directly related to the water surface elevation. Isolines of the computed distribution of ν_t^v, ν_t^{2D}, ν_t^h, k, $\overline{k}$, ε, and $\overline{\varepsilon}$ are shown in Figures F.5-F.6. The transport of the turbulence generated by horizontal shear is shown to die out slowly as mentioned before. The predicted 2D eddy viscosity is almost constant through the harbour, which explains the similar solutions for the TLS model and the TRISULA model with constant eddy viscosity. To stress that a standard first order scheme for discretizing advective terms should not be used in multi-dimensional situations, the distribution of $\overline{k}$ using this method is compared to the more accurate method which discretizes advective terms along streamlines in Figure F.7. The artificial cross-wind diffusion related to first order differencing smears out the solution, causing the turbulence to die out rapidly. This numerical side-effect is most distinct in regions where the flow crosses the grid cells under a considerable angle, which is the case near the corners of the harbour. This becomes clear if we consider the lower left corner of the harbour, where turbulence is not "capable" of crossing the corner, whereas it clearly can when derivatives are determined along streamlines. Absence of $\overline{k}$ in a large part of the harbour area results in no horizontal transfer of momentum other than generated by bottom turbulence in this region. Although there is no large difference between the development of the mixing layer in both approximations, the gross underestimation of TKE in the harbour causes too small a horizontal eddy viscosity ν_t^h in a large area. Lack of momentum transfer in horizontal directions yields local maxima, and secondary gyres can be generated leading to physically unrealistic flow patterns. From this point of view it might be important to use a conservative scheme.

Comparing results from the different two approaches on the coarse and dense grids, differences in the solution were less pronounced in case of the constant eddy viscosity. This is caused by the fact that the eddy viscosity in the TLS model is calculated and strongly depends on local velocity gradients which by definition are calculated more accurately if a small grid spacing is used. In case of the coarse grid, the mixing layer is modelled by only a few grid cells, hence velocity gradients are not represented correctly. Refining the grid, the two solutions tend to converge as shown above. A major disadvantage of the grid refinement needed for the TLS model, is the increasing computing costs involved. However, it is believed that grid refinement is only needed in areas of large horizontal velocity gradients, hence a substantial reduction in CPU time can be achieved without loosing much accuracy. It is noted that the increase in CPU time needed for the additional depth-averaged turbulence model is negligible

compared to the other numerical operations.

4.2 Modelling yacht harbour "'t Steel"

The performance of the TLS turbulence model is examined for a more realistic geometry in this section. The absence of vertical walls reduces errors due to the hydrostatic pressure approximation. However, other uncertainties, caused by the complex geometry, are introduced. Despite rather detailed information on the bathymetry, after digitization the bathymetry in the numerical model deviates from the physical model, which may have a significant influence on computed flow patterns. Furthermore, a curvilinear grid is used in order to represent land boundary as accurately as possible. In some regions occurrence of a so-called stair-case boundary cannot be avoided. It is known that this introduces computational errors. All computations were carried out on a grid consisting of 81 x 75 grid points, see Figure F.8, of which about 2/3 is active. The coordinate system referred to in the following section, is also drawn in this figure. The positive x-axis is in the direction of the flow in the river. In the vertical direction, 10 layers, similarly distributed as in the previous case, were used.

4.2.1 Results

Computations for the yacht harbour without sill were carried out with the standard k-ε model and the TLS turbulence model only; the TRISULA model with the constant horizontal eddy viscosity is left out of consideration.

The digitized bathymetry is shown in Figure F.9. In TRISULA, the vertical coordinate is made dimensionless by adopting a so-called σ-transformation:

$$\sigma = \frac{z - \zeta}{h}, \quad -1 \leq \sigma \leq 0 \tag{4.2}$$

where z is the vertical coordinate related to some reference plane, ζ is the water elevation and h is the local water depth. This yields a constant number of layers in the numerical model and the thickness of the layers depends upon the local water depth. In order to compare to computations, the measured velocities were projected on such σ-planes by linear interpolation. Vector fields in the mixing layer at $\sigma = -.075$ are compared with PTV data in Figures F.10-F.11. Strictly speaking, this comparison is not correct since velocities from measurements are situated at $\sigma = 0$. However, velocity gradients in the vertical direction are rather small near the free surface at most places and therefore comparison with PTV data is admissible. In the mixing layer the velocities obtained with the TLS turbulence model and the standard model are quite different. In contrast with the standard model, which underestimates velocities in the mixing layer, the TLS model predicts both magnitude and direction of the velocities more accurately.

In Figures F.12-F.14 the computed horizontal Reynolds shear stresses per unit mass, $\overline{u'v'}$, at three transects (at $x = 4.9$ m, 5.15 m and 5.4 m) at a depth of 5 cm below the free water surface, are plotted together with measured Reynolds shear stresses. The "wiggles", for example at the river side of the large peak are due to post-processing. The horizontal errorbars indicate the possible errors involved in mapping the measured data to the computational grid.

vertical errorbars indicate a relative error in measuring turbulent stresses of 10% as pointed out in chapter 3 (assuming that the relative error in measuring turbulent shear stresses is the same as in measuring normal stresses). The horizontal Reynolds shear stresses are in better agreement with measurements in the TLS model compared to the standard model, although the measuring grid is too coarse to draw any definite conclusions about the correctness of the computed Reynolds stresses. The lower Reynolds stresses in case of the standard model explains the underestimation of the velocities in the mixing layer.

The width of the secondary mixing layer is rather small causing the sample points to lie outside the mixing layer at $x = 5.15$ m. and $x = 5.4$ m. This seems not to be the case at $x = 4.9$ m, yielding a larger peak value for the Reynolds stress than observed at the other two transects. This makes it difficult to judge the computed Reynolds shear stresses in the secondary mixing layer, although it can be seen that the maximum stress is underestimated at $x = 4.9$ m.

The pancake-like quasi-two-dimensional turbulent structures that were observed yield horizontal Reynolds shear stresses that remain relatively large near to the free surface, something that can also be found in the TLS model but which is absent in the standard turbulence model, see Figure F.15. Towards the bottom there is a clear tendency of the stresses to decrease, indicating that the flow is not entirely 2D, as expected, which is also found in the computations.

In Figures F.16-F.17 velocities at mid-depth in the primary gyre are plotted together with LDA measurements. Despite the good agreement in the mixing layer, velocities in the harbour entrance, downstream of the stagnation point, are underestimated significantly by both models. As a consequence, velocities in the secondary mixing layer have the same tendency. Note that the centre and the shape of the gyre is predicted correctly by the TLS model only.

The local rather crude representation of the physical boundary line by a stair case grid may be the major cause of the underestimation of the velocities. It is known that such boundaries introduce additional friction and therefore decelerate the flow. Furthermore, the turbulent kinetic energy generated near the stagnation point may be overestimated, which is a well-known imperfection of the k-ε turbulence model. Because of the large velocity gradients in this area, high turbulent intensities are predicted by the model although near a stagnation point the deformation is nearly irrotational. Ultimately, this leads to exaggeration of the horizontal eddy viscosity (shown in Figure F.18), in spite of the fact that the dissipation of turbulent kinetic energy of the large-scale turbulence is overestimated in the TLS turbulence (see chapter 2). Visual observations revealed that the large scale turbulence no longer exists in the harbour region; the level of turbulence is very low and the turbulence is of a three-dimensional nature. Therefore, the horizontal eddy viscosity values are too high in the harbour.

The orientation of the secondary mixing layer is predicted incorrectly by both models, see Figures F.19-F.20. Since the flow is spread out over a large area, instead of being concentrated near the wall downstream of the secondary mixing layer, the computed velocities deviate strongly from the measurements. This plays an important role in the incorrect prediction of the position of the second stagnation point as well. It is not clear to what extent this discrepancy can be ascribed to the turbulence model used.

Throughout the entire remaining part of the harbour, the computed velocities are too low,

although velocities have increased about 35% on an average by applying the TLS turbulence model compared to the standard k-ε turbulence model. The underestimation of the Reynolds shear stresses in the secondary mixing layer seems to be of major importance for this matter.

The situation with the sill in the harbour entrance is treated in less detail, because the conclusions drawn in the previous case also apply to this situation. Besides, less data for comparison is available since no PTV measurements were carried out for this case. The same grid as before was used and the bathymetry was adapted as shown in Figure F.21.

The sill in the harbour entrance was designed for reducing the exchange of mass and, as a result, the siltation rate of the yacht harbour (Van Schijndel, 1997). Introducing this sill has a pronounced effect on the local flow field and the exchange of mass from the river to the harbour. In Figure F.22, LDA measurements for both the situation with and without the sill at the fifth σ-layer are plotted. In and near the primary mixing layer, where the influence of the sill is negligible, velocities are comparable to those discussed before. However, when the flow reaches the sill, it is deflected from its original path and is directed along the sill. This has a major effect on the position and orientation of the secondary mixing layer, on the shape of the gyre and velocities. The gyre is forced to move towards the river, yielding a more elliptic shape of the gyre since it is arrested in the y-direction between the river and the sill. Besides the guiding influence of the sill, the decrease of cross-sectional area in the y-direction, and thus increase of momentum per unit mass, causes the flow to be directed more outward. This was observed in both the LDA-measurements and the numerical results, see Figure F.23 and Figure F.24. Note the difference in flow patterns in Figures F.16-F.17 and Figures F.23-F.24.

The secondary mixing layer was seen to move towards the river and tends to follow the centre line of the sill. Due to the blocking of the flow at the end of the sill, the large velocity gradients and thus the secondary mixing layer are moved towards the river. Moreover, the large turbulent structures that develop in the upper part of the water column are not restricted in horizontal direction by the sill's geometry, nevertheless tend to follow the sill's centre line. This is likely to be caused by the interaction of the arrested flow in the lower part of the water column with the more freely moving eddies near the free surface. Only a small part of the eddies, which transport the matter from the harbour entrance to the harbour, enters the harbour area, resulting in reduced siltation rates.

In the harbour itself, measured velocities decreased by 70% of the magnitude of those in the original situation (see Figure F.22), which, however, cannot be found in the results of the numerical model. This reduction cannot be related to the reduction of cross-sectional area only; the shape of the sill determines to reduction of momentum exchange to a large extent.

In the primary mixing layer, computed velocities obtained with the TLS model again agree better with measured values and in this region than the standard k-ε model. The flows in the two different geometries behave in a similar way in this region, which is also confirmed by the computed horizontal eddy viscosity in this region (Figure F.25). The large horizontal velocity gradients that were measured are not predicted correctly with the model, as in the previous case. Finally, computed and measured horizontal turbulent shear stresses, at the same transects as before, are shown in Figures F.26-F.28. Again the same conclusions as

before can be drawn.

Chapter 5

Conclusions and recommendations

A two-length-scale turbulence model was presented that is based on the well-known k-ε turbulence model. This model, which is computationally hardly more expensive than the standard model, takes non-isotropy of shallow-water turbulence into account via two separate turbulence models. The small-scale bed generated turbulence, which is essentially three-dimensional, is modelled by a 3D k-ε model in which the production of turbulent kinetic energy is determined solely by vertical velocity gradients. The larger scale quasi-two-dimensional turbulence is modelled with a depth-averaged k-ε turbulence model in which the turbulent kinetic energy is produced by horizontal velocity gradients only. The direct interaction of the two separate turbulent length scales was neglected, although it may play an important role in real-life turbulence. However, interaction via the mean flow still exists.

Summarizing the computational results for the square harbour, it can be stated that the flow in this case can be predicted reasonably well with all three turbulence models, i.e. the standard 3D k-ε model, the TRISULA model and the TLS model. However, in order to represent some details of the flow correctly, it is necessary to model the non-isotropic behaviour of the flow, reflected in the turbulence model used. This is the reason why the standard single-length-scale turbulence model fails to represent the shape of the mixing layer and the characteristic bulb in the vertical velocity profile near the stagnation point correctly. Both the constant horizontal eddy viscosity model and the TLS model seem to be more suitable for predicting this type of flow than the standard k-ε model. The disadvantage of the constant eddy viscosity to be prescribed by the user, which gives the model an empirical character, can be circumvented by using the TLS turbulence model. This is even more true when transient flows are considered or when choosing an eddy viscosity is a less trivial task. The predictive capabilities of the turbulence model increase by avoiding the empirical eddy viscosity, which is one of the advantages of this turbulence model.

A relatively fine grid was needed to obtain converged solutions, especially if no emperical value for the horizontal eddy viscosity was used. Extra work can be minimized, though, if only local grid refinement (in regions with large horizontal velocity gradients, such as in the mixing layer) is adopted, possibly with automatic grid adaptation.

Results from LDA- and PTV-experiments were used for further model testing in a more realistic geometry. It was shown that also in this geometry the standard k-ε model un-

derestimates the velocities in the mixing layer that develops between the river and harbour. Moreover, horizontal Reynolds shear stresses were predicted more correctly using the TLS turbulence model than with the standard k-ε model. Especially near the free surface, where the eddy viscosity (and therewith the Reynolds stress) goes to zero in case of the standard model, the TLS model yields horizontal Reynolds shear stresses that are in much better agreement with the measured quasi-two-dimensional turbulence.

In contrast with the square harbour, errors due to the hydrostatic pressure assumption were reduced in this situation, since the slopes of the model were much more gentle. However the complexity of the grid and bathymetry introduces additional errors, the importance of which is not clear at this moment. In this complex flow it is hard to distinguish those errors from the ones resulting from the imperfection of the turbulence model. In order to obtain more accurate results, it is expected that the grid should be refined in the vicinity of the stagnation point downstream of the primary mixing layer. The coarse representation of the boundary line, locally enhances the resistance which locally results in smaller velocities and increasing velocity gradients at the closed boundary. Furthermore, turbulent intensities near the stagnation point that are determined with a k-ε turbulence model are too high. Since the turbulence is transported into the harbour, the horizontal eddy viscosity in the harbour as computed by the depth-averaged k-ε model is likely to be overestimated, despite the presumed excessive dissipation of the large scale turbulence with this model.

Partly as a result of the abovementioned shortcomings, the computed flow field and horizontal turbulent shear stresses agree rather well with the measurements in the primary mixing layer, but results for both models are still unsatisfactory in the remaining areas of the computational domain. Qualitatively, the results of the TLS model are quite similar to the observations in the physical model; the position of the gyre and the stagnation points are predicted with sufficient accuracy. However, velocities in the secondary mixing layer, between the harbour entrance and the harbour itself, are underestimated considerably. Moreover, the direction of the flow deviates significantly from those observed in measurements in case of both the TLS and standard k-ε turbulence model. The additional resistance near the stair-case boundary and the exaggeration of the eddy viscosity are believed to be the major factors. Errors introduced by the latter effect can be reduced by relating the production turbulent kinetic energy not solely to the strain rate of the velocity field.

Computations for a situation in which a sill was placed in the harbour entrance yielded the same picture.

From the above it is clear that the TLS model needs further testing for different situations. Testing the model for the square harbour with a non-hydrostatic code can preclude any doubt about the influence of the violation of the hydrostatic pressure assumption, without loosing the transparency of a relatively simple flow. Moreover, to make the model physically more correct, a transfer term should be included in the turbulence model that accounts for the energy transfer from large to small-scale turbulence and vice versa. The performance of the model can be influenced by these terms in case of intermediate shallowness of the flow, although it is believed that in case of yacht harbour "'t Steel" the coarse grid and the gross representation of the boundary line are the major sources of inaccuracy. Testing the model for other relatively simple flows before applying it to real-live situations is recommended in order to gain insight into the model's limitations. Extension to stratified flows, in which the

density interface can act as an internal boundary and thereby induce two-dimensionality. may also be desirable and is possible in principle.

Acknowledgments

The author wishes to thank Delft Hydraulics for making available the LDA measuring equipment HILDA and the numerical model TRISULA. This research was financially supported by the Dr. ir. C. Lely Foundation.

References

BABARUTSI, S., & CHU, V. H. 1991. A two-length-scale model for quasi-two-dimensional turbulent shear flows. *Pages 53–60 of: Refined flows. Modelling*, vol. C. IAHR.

BOOIJ, R. 1986. *Measurements of Exchanges between River and Harbour (in Dutch)*. Tech. rept. 9-86. Delft Univ. of Techn.

BOOIJ, R. 1989. *Depth averaged k-ε-model in ODYSSEE*. Tech. rept. 1-89. Delft Univ. of Techn.

BOOIJ, R. 1991. Eddy viscosity in a harbour. *Pages 81–90 of: Refined flows. Modelling*, vol. C. IAHR.

BROWN, G.L., & ROSHKO, A. 1974. On density effects and large structure in turbulent mixing layers. *J. of Fluid Mech.*, **64**(4), 775–816.

DELFT HYDRAULICS. 1994. *TRISULA manual*. Delft Hydraulics. Release 2.

DURSTHOFF, W. 1970. *On the quantitative exchange between river and harbour (in German)*. Tech. rept. 34. Techn. Univ. Hannover, Germany. Mitteilungen des Franzius-Instituts für Grund- und Wasserbau der Technischen Universität Hannover.

HINZE, J. 1975. *Turbulence*. New York: Mc-Graw Hill.

KRAICHNAN, R.H. 1967. Inertial ranges in two-dimensional turbulence. *Phys. Fluids*, **10**, 1417–1423.

LANGENDOEN, E.J. 1992. *Flow patterns and transport of dissolved matter in tidal harbours*. Ph.D. thesis, Delft Univ. of Techn.

LANGENDOEN, E.J., & KRANENBURG, C. 1993. Simulation of unsteady flow in harbors. *Advances in Hydro-Science and -Engineering*, **I**, 1612–1617.

LEONARD, B. P., & DRUMMOND, J. E. 1995. Why you should not use 'hybrid', 'power-law' or related exponential schemes for convective modelling-there are much better alternatives. *Int. J. for Num. Meth. in Fluids*, **20**, 421–442.

LESIEUR, M. 1990. *Turbulence in fluids, stochastic and numerical modelling*. Dordrecht: Kluwer Academic Publishers.

NEZU, I., & NAKAGAWA, H. 1993. *Turbulence in Open-Channel Flows.* Delft, The Netherlands: International Association of Hydraulic Research.

RODI, W. 1980. *Turbulence models and their applications in hydraulics - A state of the art review.* Delft, The Netherlands: International Association of Hydraulic Research.

ROHR, F. 1933. *Movement of water and sediment in harbours on rivers and seas (in German).* Ph.D. thesis, Techn. Hochschule Karlsruhe.

SCHIESTEL, R. 1983. Sur le concept d'échelles multiples en modélisation des écoulements turbulents. *J. de Mécanique théorique et appliquée*, **2**(3), 417–449.

TENNEKES, H. & LUMLEY, J.L. 1972. *A first course in turbulence.* Cambridge, Massachusetts: MIT Press.

TUKKER, J. 1997. *Turbulence structures in shallow free-surface mixing layers.* Ph.D. thesis. Delft Univ. of Techn.

UIJTTEWAAL, W.S.J., & TUKKER, J. 1997. Development of quasi 2-D structures in shallow free-surface turbulence with lateral shear. *Submitted to: Exp. in Fluids.*

UITTENBOGAARD, R.E., VAN KESTER, J.A.TH.M., & STELLING, G.S. 1992. *Implementation of three turbulence models in TRISULA for rectangular horizontal grids.* Tech. rept. Z162. Delft Hydraulics Laboratory.

VAN KESTER, J.A.TH.M. 1994. *Validation of DELFT3D for mixing layer test. Phase 1: improved implementation k-ε model (in Dutch).* Tech. rept. Z810. Delft Hydraulics Laboratory.

VAN NOORT, E.T.L. 1997. *PTV in a shallow-water mixing layer (in preparation).* M.Sc. thesis, Delft Univ. of Techn.

VAN SCHIJNDEL, S.A.H. 1997. *Siltation of a river harbour (in Dutch).* M.Sc. thesis. Delft Univ. of Techn.

VOLLMERS, H.J. 1963. *Systematics of the measures to decrease the sedimentation of suspension in harbours on rivers (in German).* Ph.D. thesis, Techn. Hochschule Karlsruhe.

VREUGDENHIL, C.B., & KOREN, B. (eds). 1993. *Numerical methods for advection-diffusion problems.* Notes on numerical fluid mechanics. Vieweg, Braunschweig, Wiesbaden.

WESTRICH, B. 1977. *Exchange of mass in steady flows with dead zones (in German).* Tech. rept. SFB 80 ET/80. Techn. Univ. Karlsruhe, Germany.

List of Figures

2.1 Definition of staggered grid 13

3.1 Adapted physical scale model of yacht harbour "'t Steel". Bottom heights in cm above datum level. 16
3.2 Laser Doppler anemometer HILDA with bell attached to it 17
3.3 Measuring grid. Letters R and M indicate positions in river and mixing layer. respectively 20
3.4 Autocorrelationfunction of the transverse velocity fluctuations (v') in the river (R) and mixing layer (M); location R and M are shown in Figure 3.3. 22
3.5 Top view of the shallow-water mixing layer and the approximate flow pattern. Four (developing) quasi 2D structures and a gyre can be discerned. The width of the harbour entrance is approximately 10 times the average water depth. . 23
3.6 One-dimensional power-density spectrum of transverse velocity fluctuations (v') in the river and mixing layer 25

4.1 Definition sketch of square harbour 27

F.1 Computational grid for square (1x1 m^2) harbour (88x64 grid points). 44
F.2 Velocity profiles along two transects through the measured centre of the gyre: a) 0.015, b) 0.04, c) 0.06 and d) 0.08 m above the bottom. Measured: •, 3D k-ε model with production term according to eq. (4.1): small dashes, 3D k-ε model with production term according to eq. (2.9a) and ν_t^{2D}= 5x10^{-4} m^2/s: large dashes , TLS turbulence model: solid line. 45
F.3 Vertical distribution of the horizontal velocity components at P. Measured: •, 3D k-ε model with production term according to eq. (4.1): small dashes, 3D k-ε model with production term according to eq. (2.9a) and ν_t^{2D}= 5x10^{-4} m^2/s: large dashes , TLS turbulence model: solid line. 46
F.4 Computed vector fields with the TLS model at each computational layer. Layer 1 is near the surface and layer 10 near the bottom. The last picture represents the water surfuce elevation to which the stagnation points can be related. . . 48
F.5 Isolines of ν_t^v (m^2/s), k (m^2/s^2), and ε (m^2/s^3), from top to bottom, in the square harbour at 51% of the water depth. 49
F.6 Isolines of ν_t^{2D} (m^2/s), $\overline{k}$ (m^2/s^2), and $\overline{\varepsilon}$ (m^2/s^3), from top to bottom, in the square harbour. 50

F.7 Isolines of $\overline{k}$ in harbour for the first order upwind along streamlines (top) and standard first order upwind method (bottom). $\overline{k}$=0.0002. 0.0006. 0.0010. 0.0014. 0.003 and 0.005 m^2/s^2 51
F.8 Grid used for modelling yacht harbour "'t Steel" (81x75 grid points). 52
F.9 Isolines of depth, situation without a sill in the harbour entrance. 53
F.10 Velocity vectors at the mixing layer between river and harbour entrance computed with the TLS model (thin arrows) and PTV measurements (thick arrows) at $\sigma = -.075$ and $\sigma = 0$, respectively. Situation without sill in harbour entrance. 54
F.11 Velocity vectors at the mixing layer between river and harbour entrance computed with the standard k-ε model (thin arrows) and PTV measurements (thick arrows) at $\sigma = -.075$ and $\sigma = 0$, respectively. Situation without sill in harbour entrance. 55
F.12 Reynolds shear stress per unit mass at x=4.9 m and z=-0.05 m. Situation without sill in harbour entrance. 56
F.13 Reynolds shear stress per unit mass at x=5.15 m and z=-0.05 m. Situation without sill in harbour entrance. 56
F.14 Reynolds shear stress per unit mass at x=5.4 m and z=-0.05 m. Situation without sill in harbour entrance. 57
F.15 Reynolds shear stress per unit mass at x=5.15 m and y=-1.1 m as a function of depth z. Situation without sill in harbour entrance. 57
F.16 Velocity vectors at the harbour entrance computed with the TLS model (thin arrows) and LDA measurements (thick arrows) at $\sigma = -.51$. Situation without sill in harbour entrance. 58
F.17 Velocity vectors at the harbour entrance computed with the standard k-ε model (thin arrows) and PTV measurements (thick arrows) at $\sigma = -.51$. Situation without sill in harbour entrance. 59
F.18 Horizontal eddy viscosity ν_t^{2D} (m^2/s) computed by the TLS model. Situation without sill in harbour entrance. 60
F.19 Velocity vectors in the harbour entrance computed with the TLS model (thin arrows) and PTV measurements (thick arrows) at $\sigma = -.075$ and $\sigma = 0$, respectively. Situation without sill in harbour entrance. 61
F.20 Velocity vectors in the harbour computed with the standard k-ε model (thin arrows) and PTV measurements (thick arrows) at $\sigma = -.075$ and $\sigma = 0$, respectively. Situation without sill in harbour entrance. 62
F.21 Isolines of depth, situation with a sill in the harbour entrance. 63
F.22 Comparison of mean velocities at $\sigma = -.51$, obtained with LDA, in situation with (thick arrows) and without (thin arrows) a sill in the harbour entrance. 64
F.23 Velocity vectors at the harbour entrance computed with the TLS model (thin arrows) and LDA measurements (thick arrows) at $\sigma = -.51$. Situation with sill in harbour entrance. 65
F.24 Velocity vectors at the harbour entrance computed with the TLS model (thin arrows) and LDA measurements (thick arrows) at $\sigma = -.51$. Situation with sill in harbour entrance. 66

F.25 Horizontal eddy viscosity ν_t^{2D} (m^2/s) computed by the TLS model. Situation with sill in harbour entrance. 67
F.26 Reynolds shear stress per unit mass at x=4.9 m and z=-0.05 m. Situation with sill in harbour entrance. 68
F.27 Reynolds shear stress per unit mass at x=5.15 m and z=-0.05 m. Situation with sill in harbour entrance. 68
F.28 Reynolds shear stress per unit mass at x=5.4 m and z=-0.05 m. Situation with sill in harbour entrance. 69

Figures

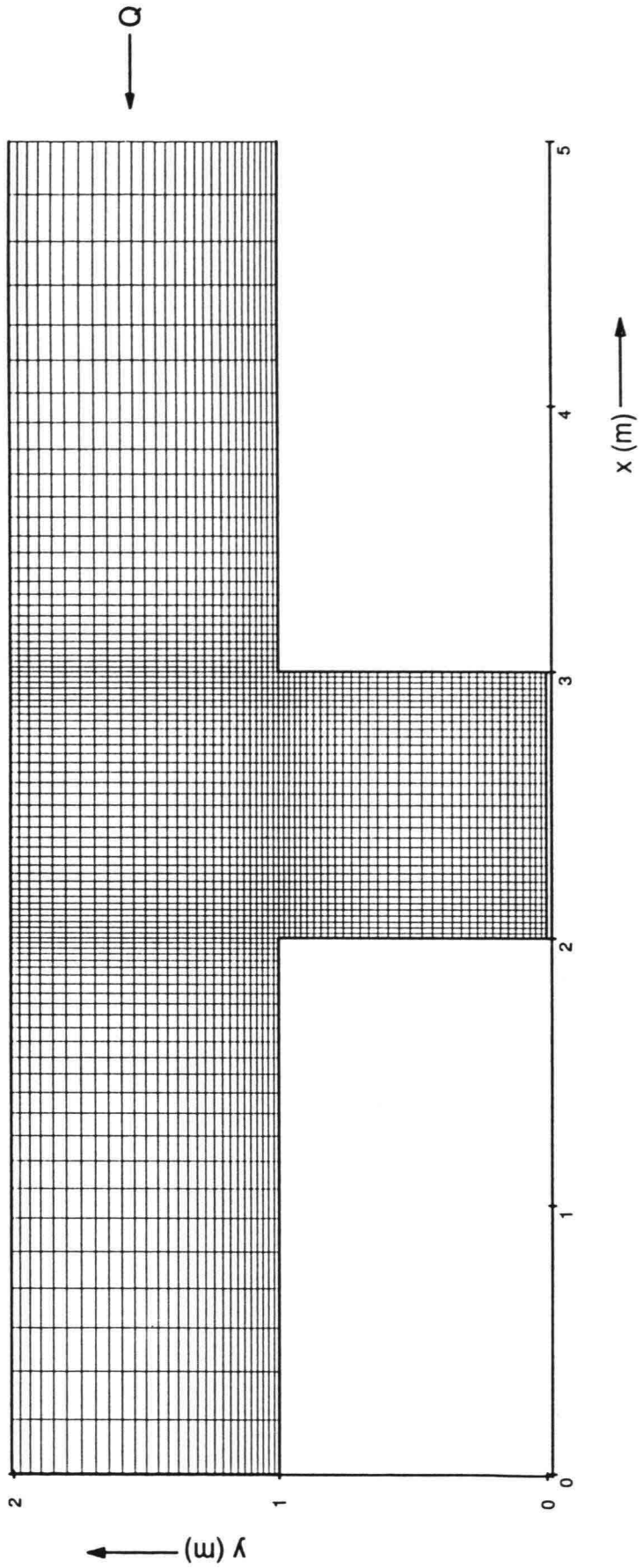

Figure F.1: Computational grid for square (1x1 m^2) harbour (88x64 grid points).

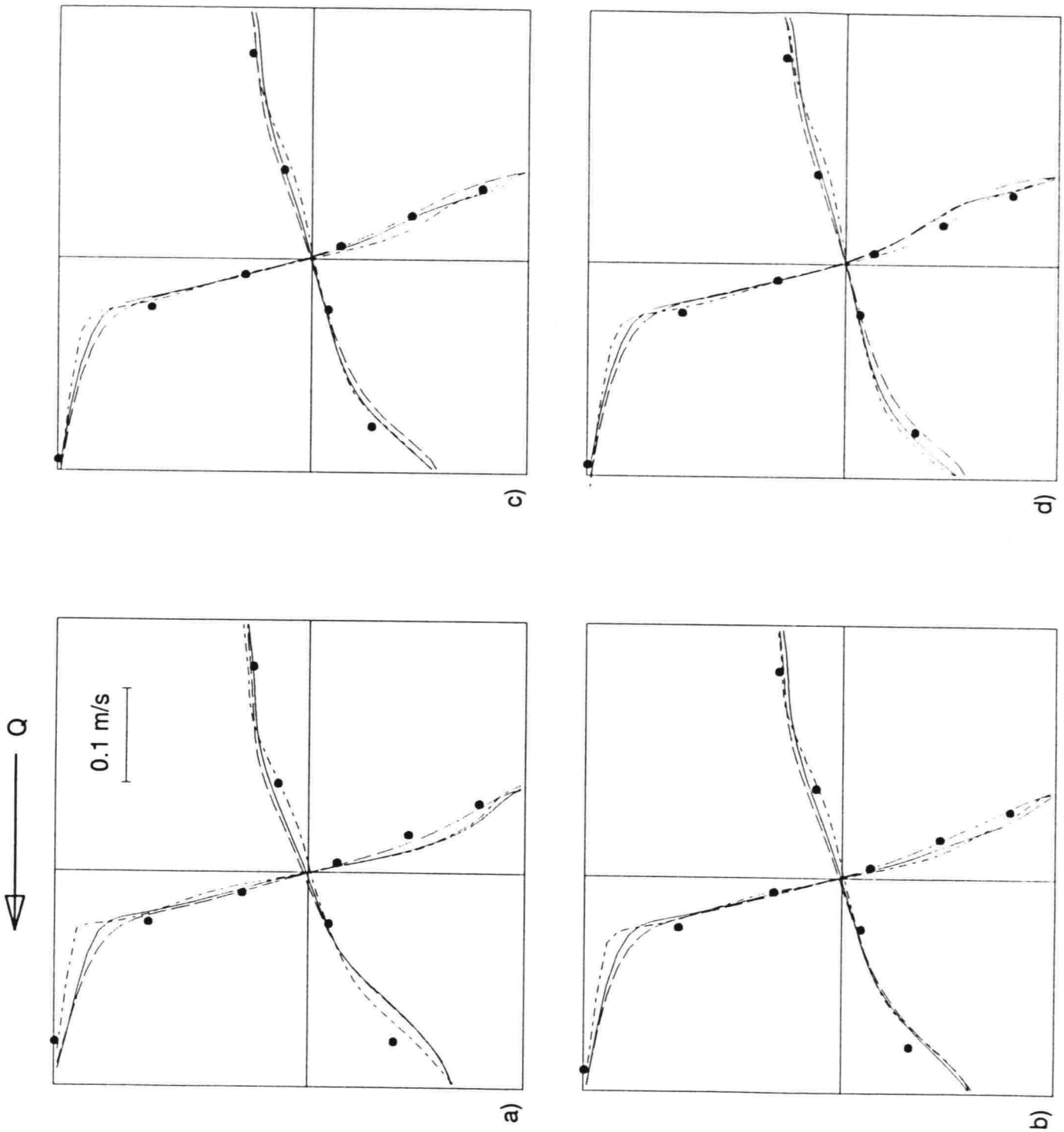

Figure F.2: Velocity profiles along two transects through the measured centre of the gyre: a) 0.015, b) 0.04, c) 0.06 and d) 0.08 m above the bottom. Measured: •, 3D k-ε model with production term according to eq. (4.1): small dashes, 3D k-ε model with production term according to eq. (2.9a) and ν_t^{2D}= 5x10^{-4} m^2/s: large dashes , TLS turbulence model: solid line.

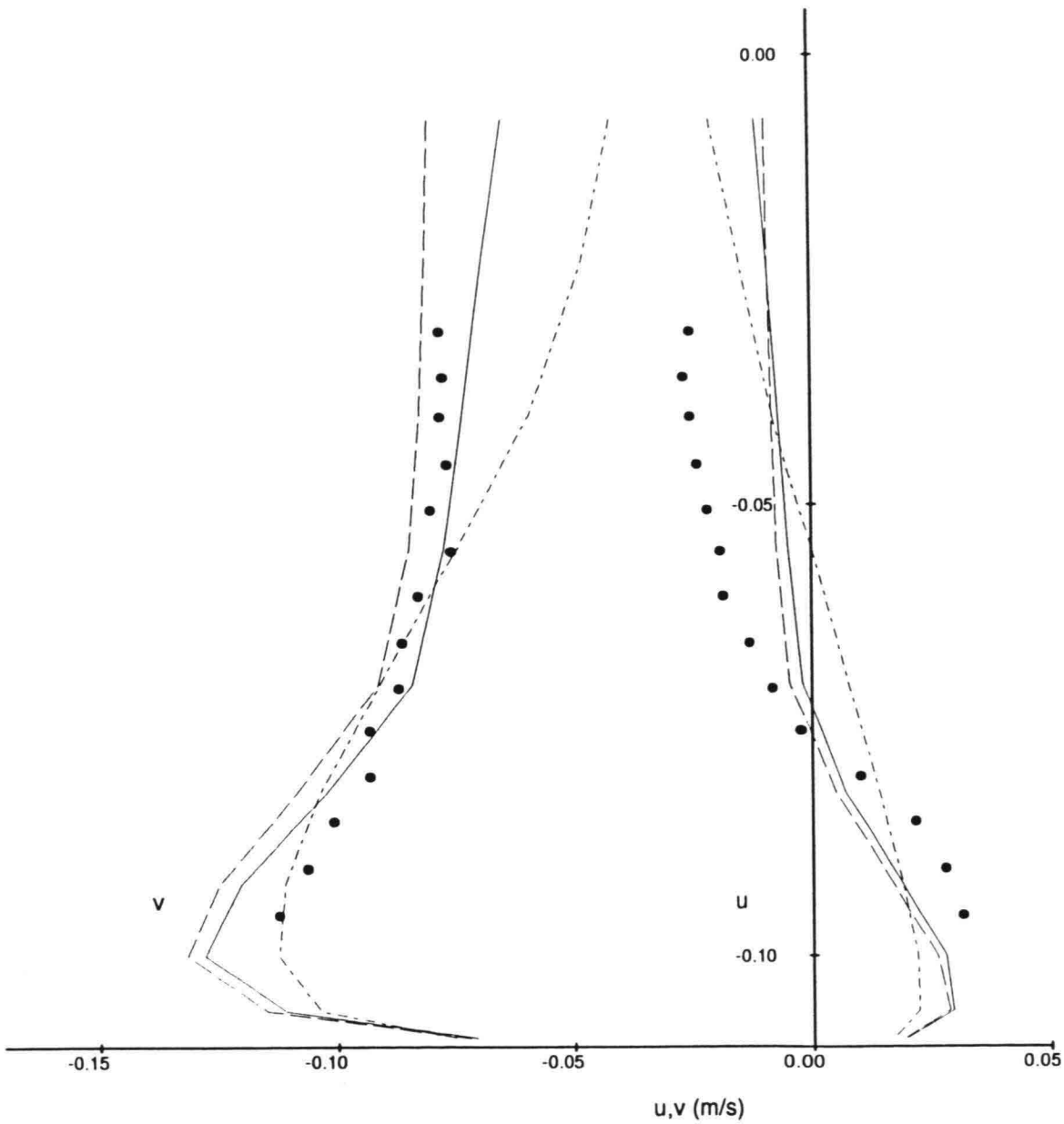

Figure F.3: Vertical distribution of the horizontal velocity components at P. Measured: •, 3D k-ε model with production term according to eq. (4.1): small dashes, 3D k-ε model with production term according to eq. (2.9a) and ν_t^{2D}= 5x10^{-4} m^2/s: large dashes , TLS turbulence model: solid line.

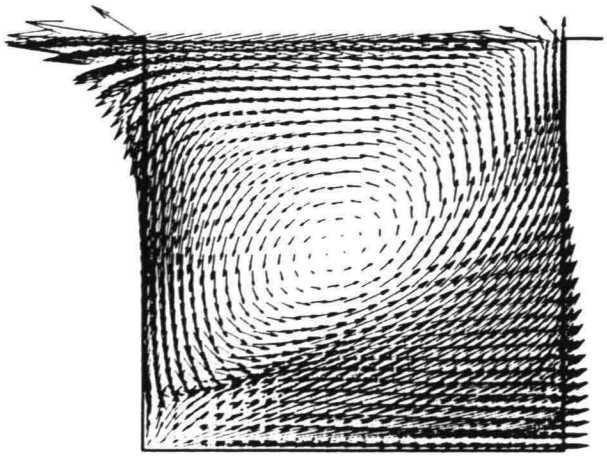

layer 1

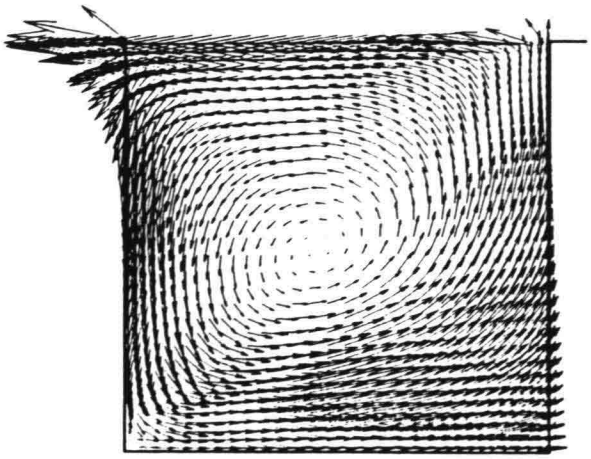

layer 2

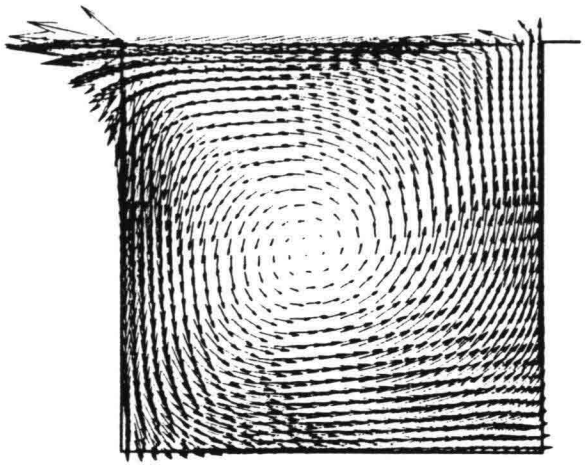

layer 3

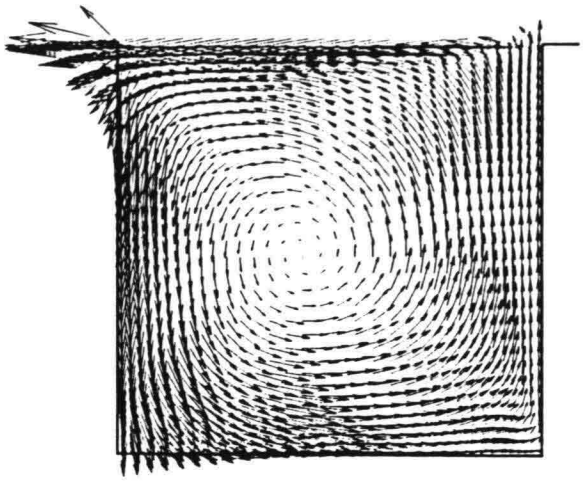

layer 4

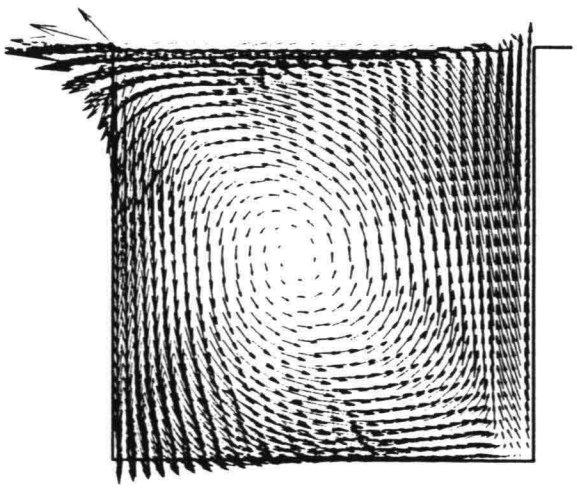

layer 5

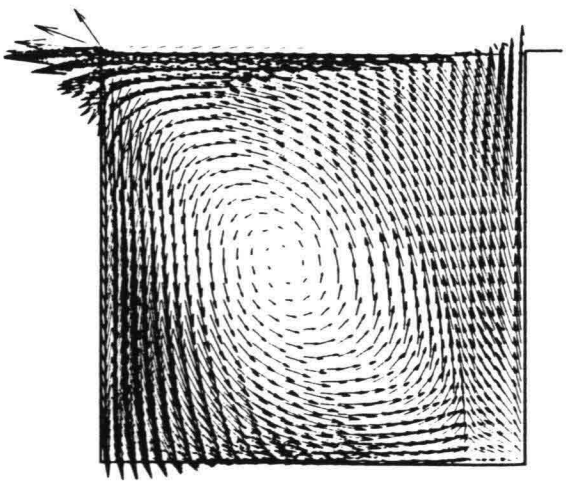

layer 6

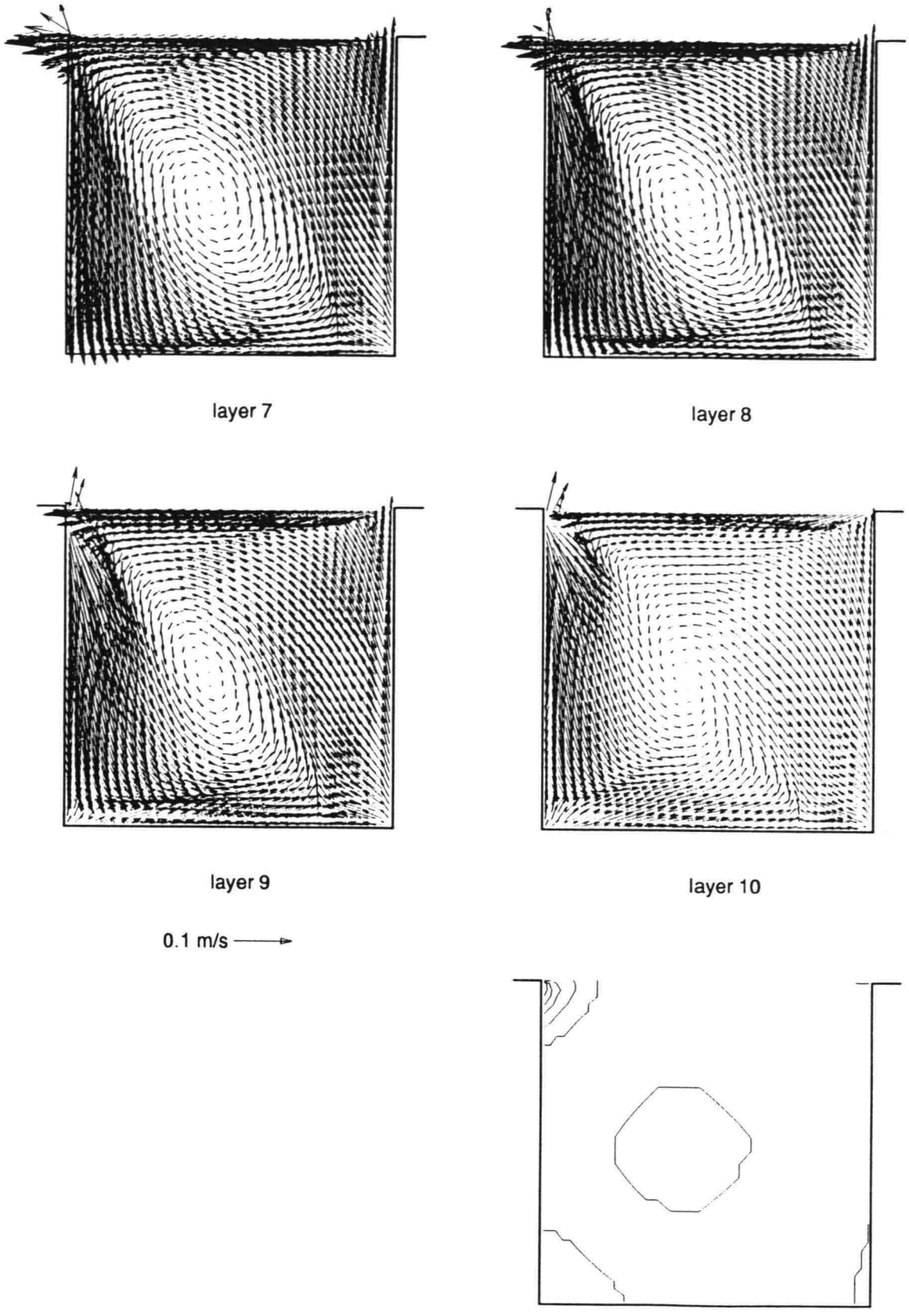

Figure F.4: Computed vector fields with the TLS model at each computational layer. Layer 1 is near the surface and layer 10 near the bottom. The last picture represents the water surfuce elevation to which the stagnation points can be related.

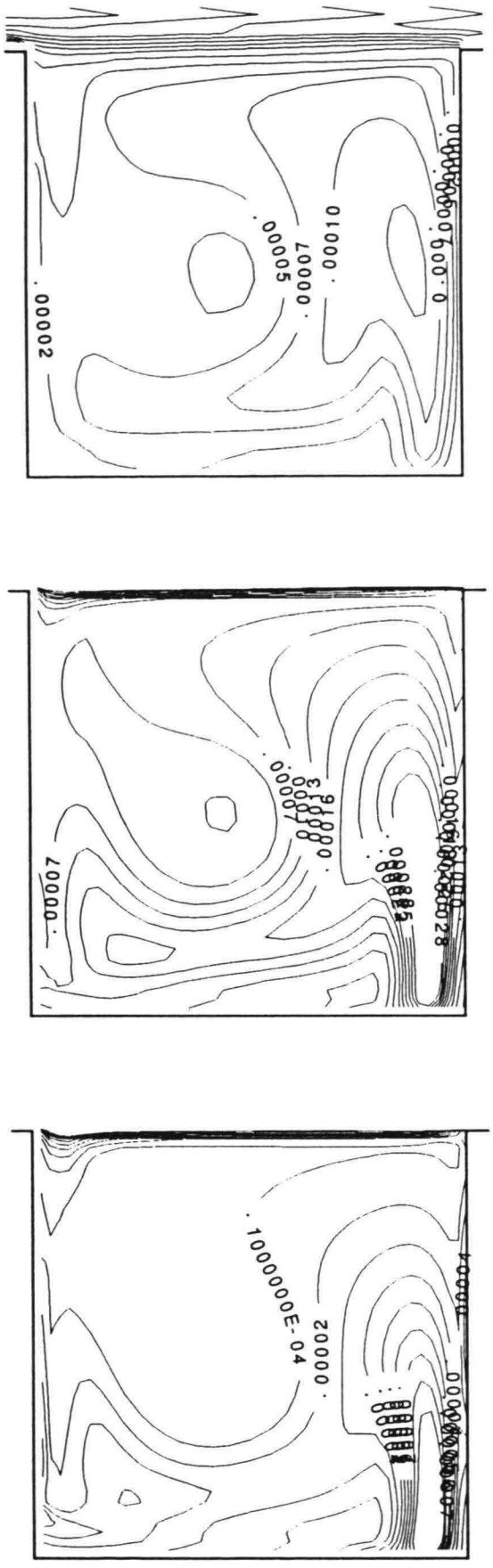
.00002
.00005
.00007
.00010
.00007
.00010
.00013
.00016
.00019
.00022
.00025
.00028
.00031
.00034
.00037
.00040
.00043
.00046
.00049
.00052
.00055
.00058
.00061
.00064
.00067
.00070
.00073
.00076
.00079
.00082
.00085
.00088
.00091
.00094
.00097
.00100
.00103
.00106
.00109
.00112
.00115
.00118
.00121
.00124

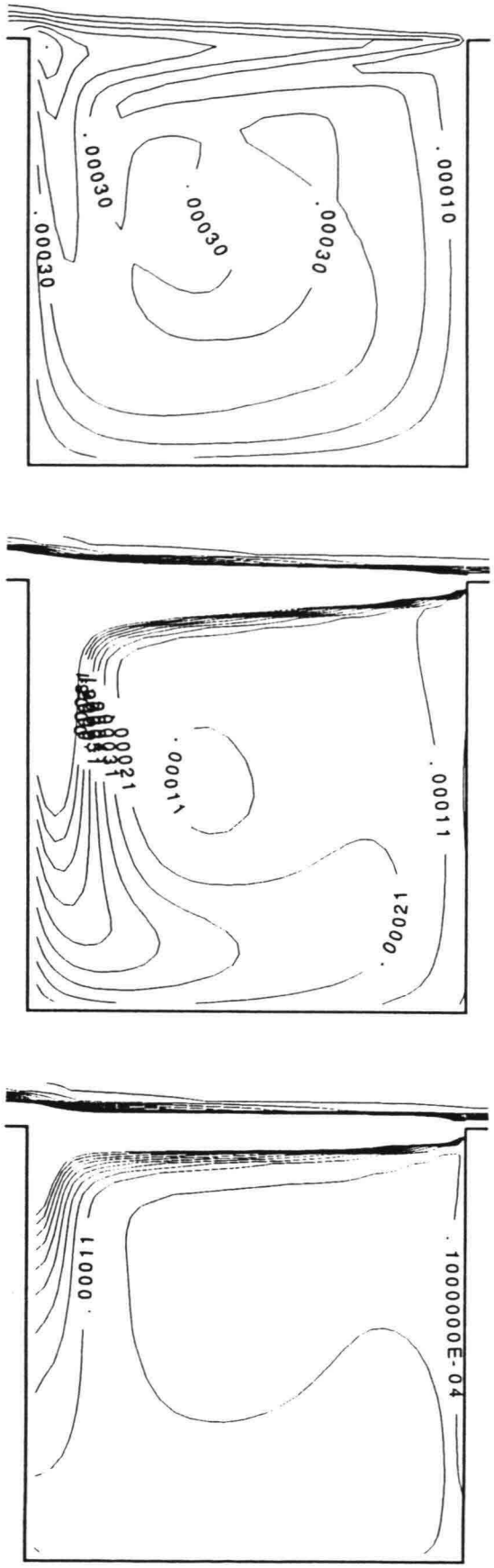

Figure F.6: Isolines of ν_t^{2D} (m^2/s), $\overline{k}$ (m^2/s^2), and $\overline{\varepsilon}$ (m^2/s^3), from top to bottom, in the square harbour.

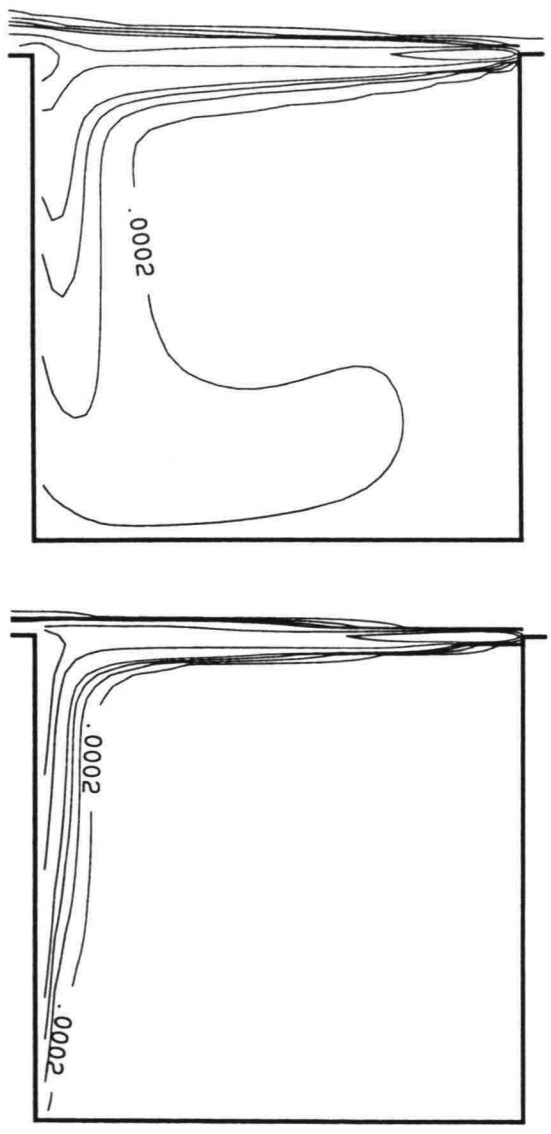

Figure F.7: Isolines of $\overline{k}$ in harbour for the first order upwind along streamlines (top) and standard first order upwind method (bottom). $\overline{k}$=0.0002, 0.0006, 0.0010, 0.0014, 0.003 and 0.005 m^2/s^2

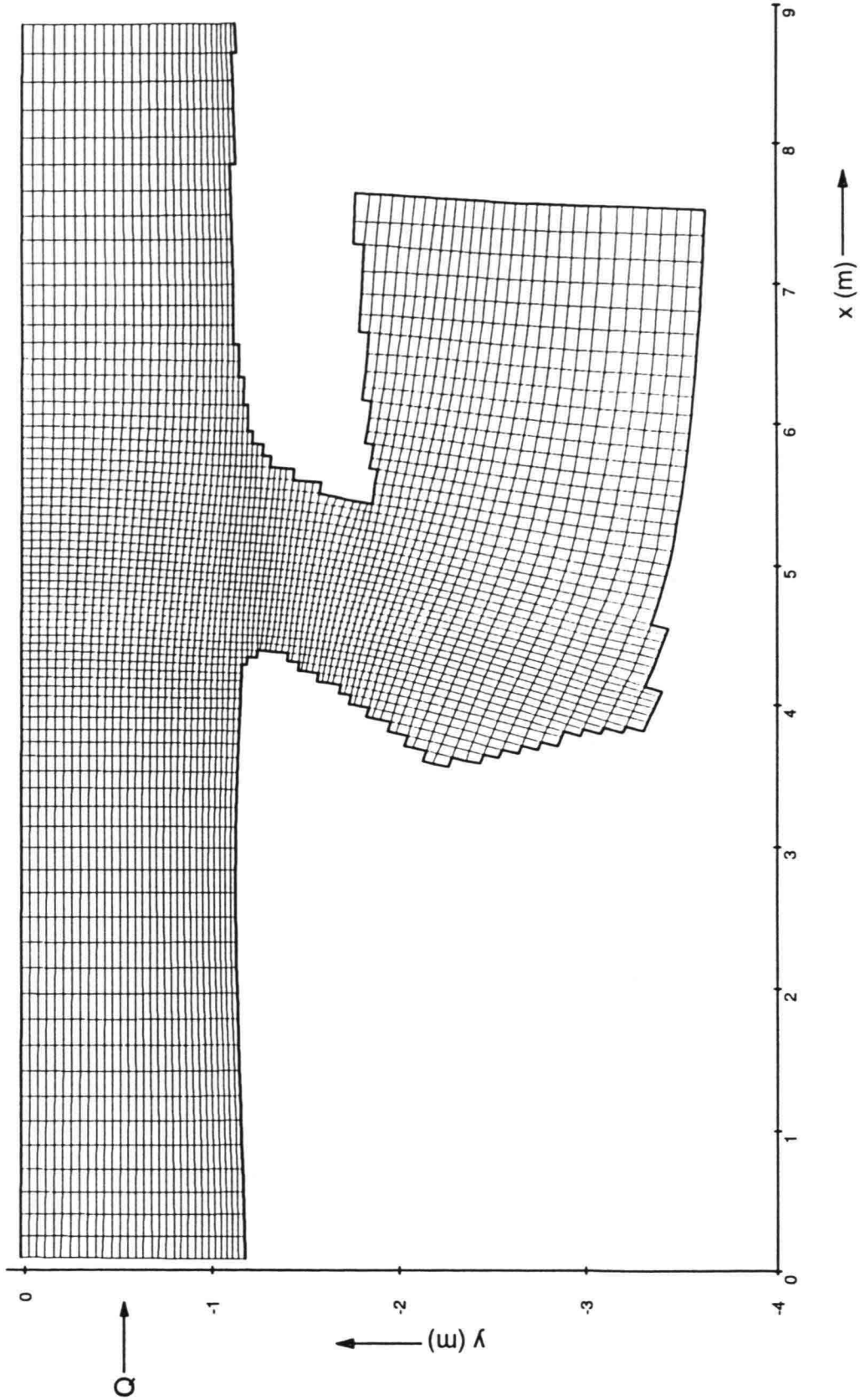

Figure F.8: Grid used for modelling yacht harbour "'t Steel" (81x75 grid points).

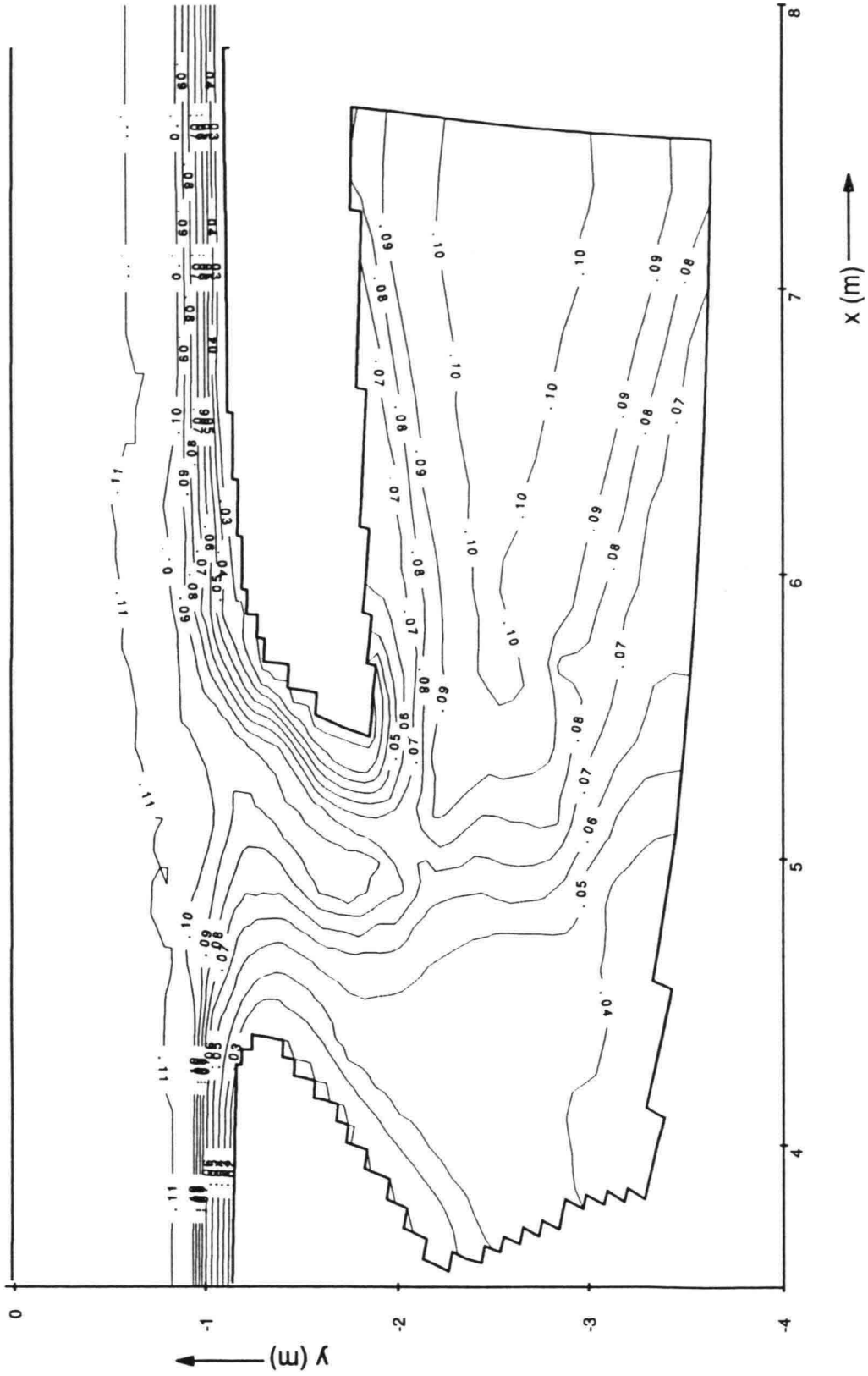

Figure F.9: Isolines of depth, situation without a sill in the harbour entrance.

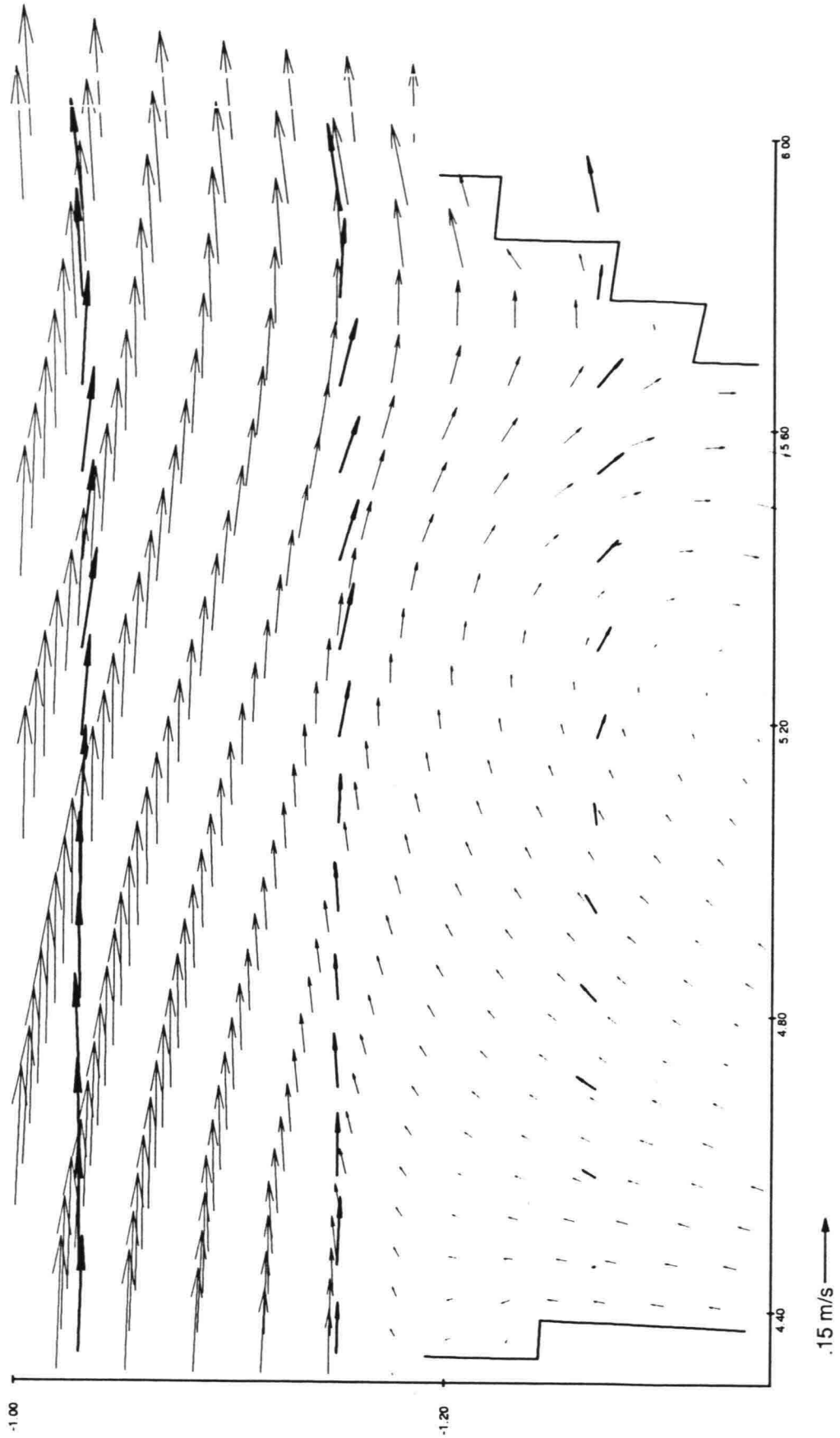

Figure F.10: Velocity vectors at the mixing layer between river and harbour entrance computed with the TLS model (thin arrows) and PTV measurements (thick arrows) at $\sigma = -.075$ and $\sigma = 0$, respectively. Situation without sill in harbour entrance.

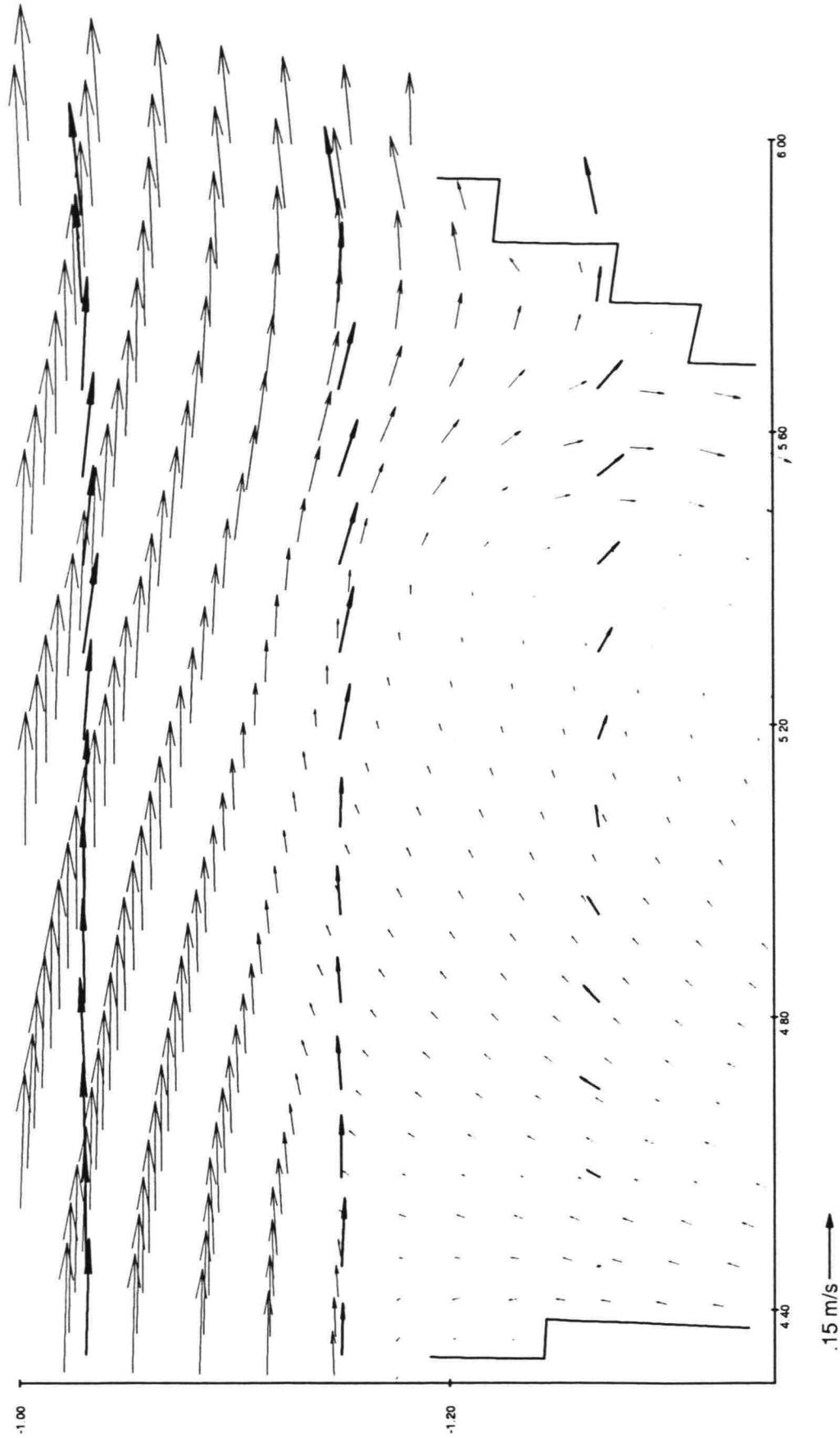

Figure F.11: Velocity vectors at the mixing layer between river and harbour entrance computed with the standard k-ε model (thin arrows) and PTV measurements (thick arrows) at $\sigma = -.075$ and $\sigma = 0$, respectively. Situation without sill in harbour entrance.

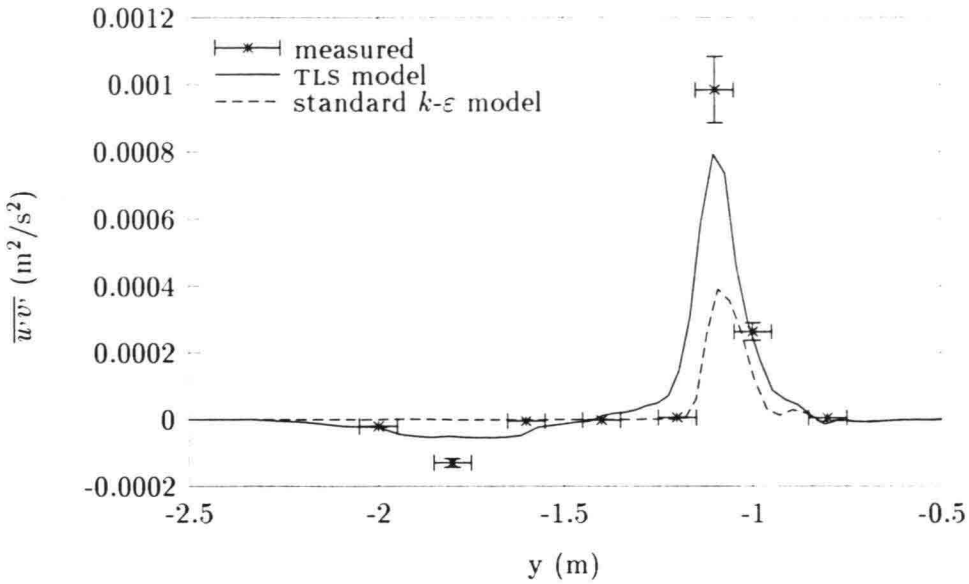

Figure F.12: Reynolds shear stress per unit mass at x=4.9 m and z=-0.05 m. Situation without sill in harbour entrance.

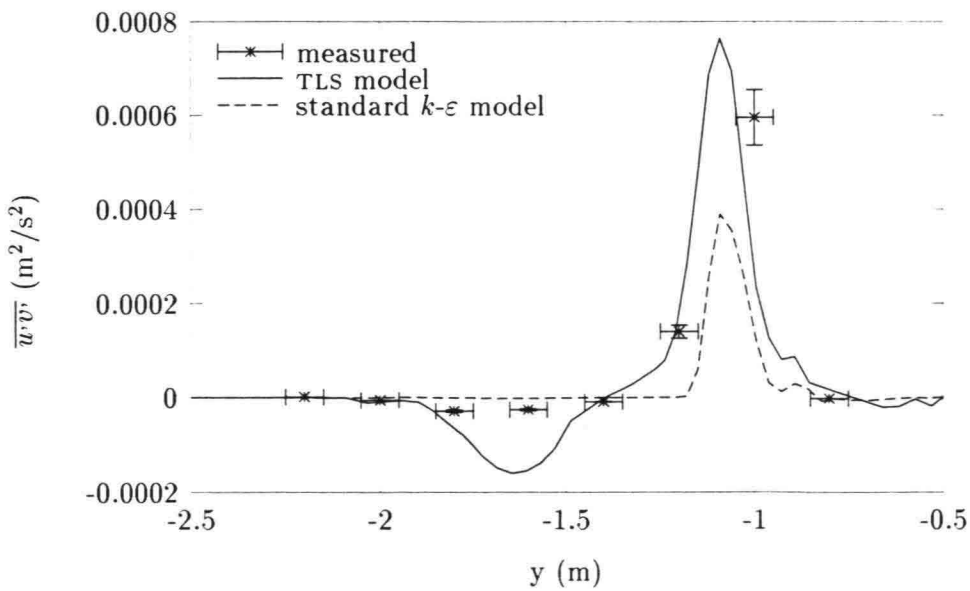

Figure F.13: Reynolds shear stress per unit mass at x=5.15 m and z=-0.05 m. Situation without sill in harbour entrance.

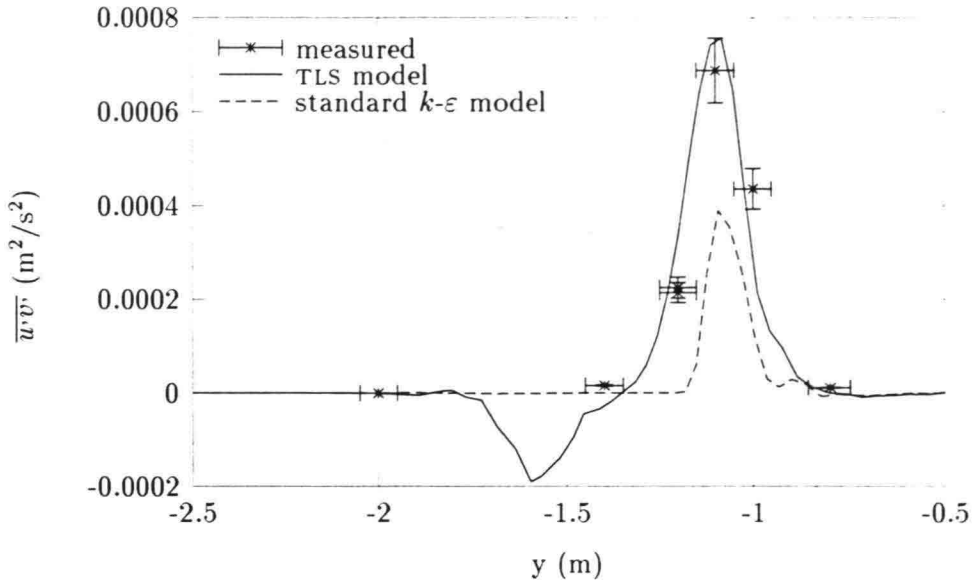

Figure F.14: Reynolds shear stress per unit mass at x=5.4 m and z=-0.05 m. Situation without sill in harbour entrance.

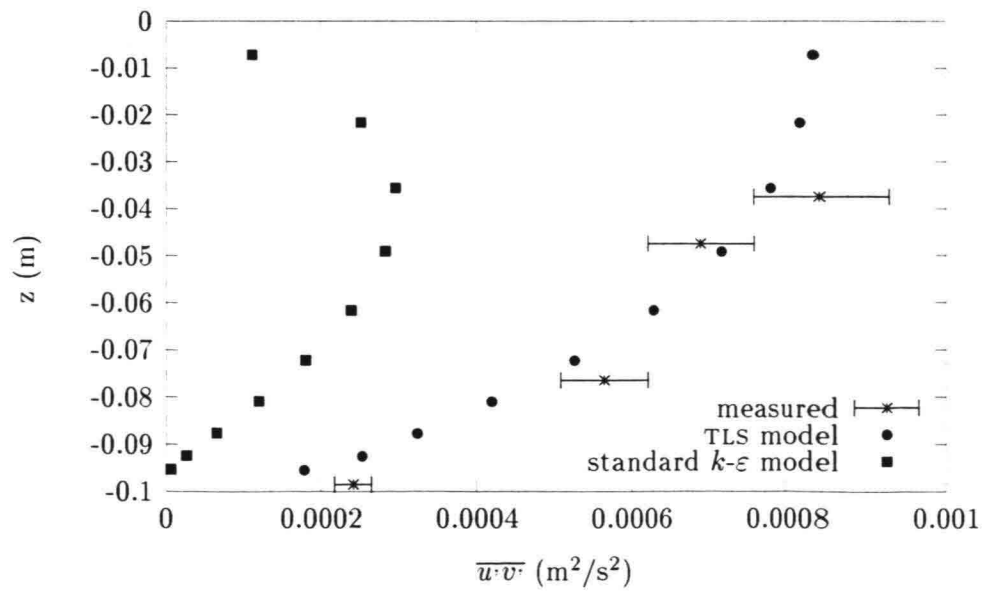

Figure F.15: Reynolds shear stress per unit mass at x=5.15 m and y=-1.1 m as a function of depth z. Situation without sill in harbour entrance.

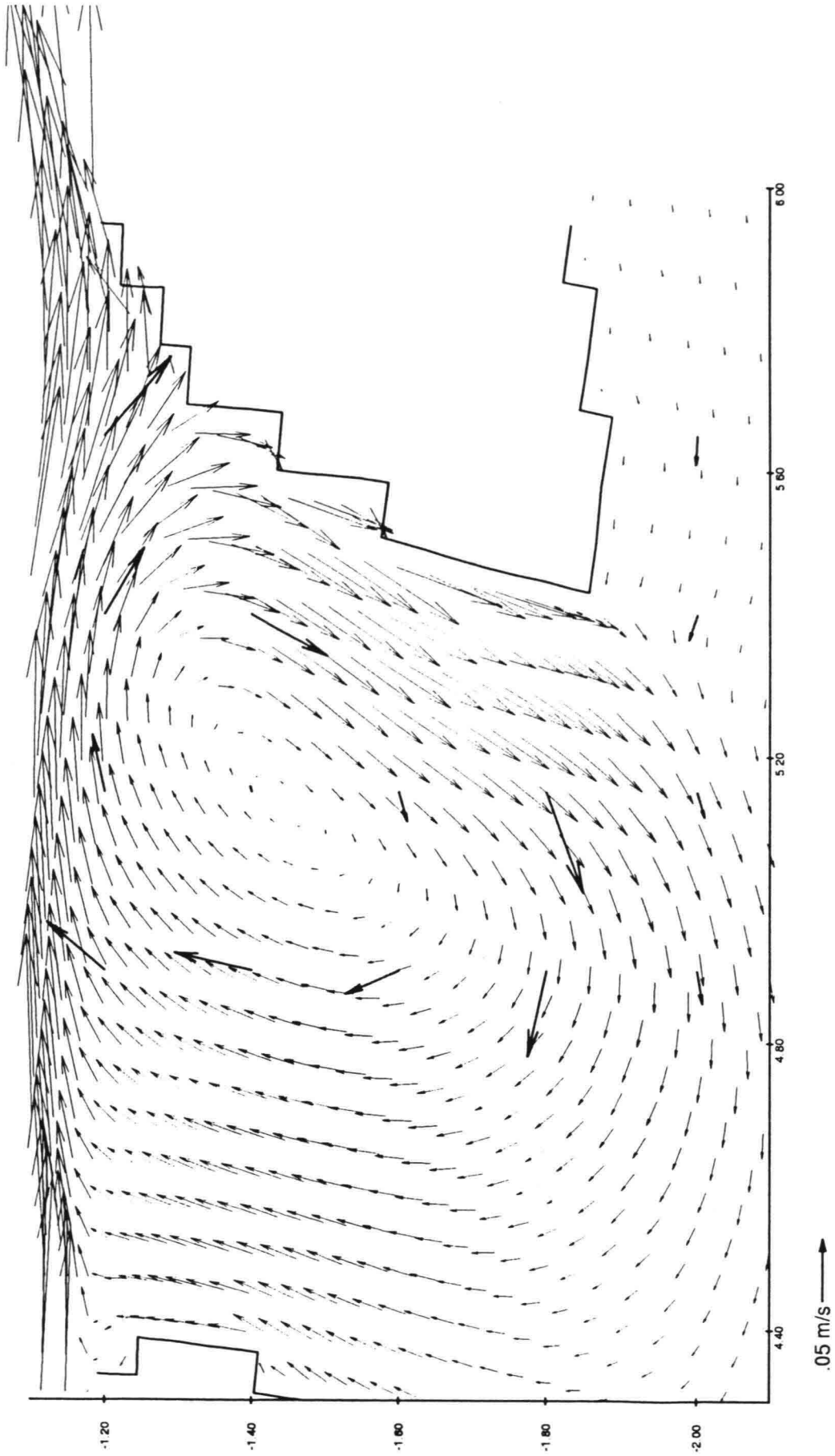

Figure F.16: Velocity vectors at the harbour entrance computed with the TLS model (thin arrows) and LDA measurements (thick arrows) at $\sigma = -.51$. Situation without sill in harbour entrance.

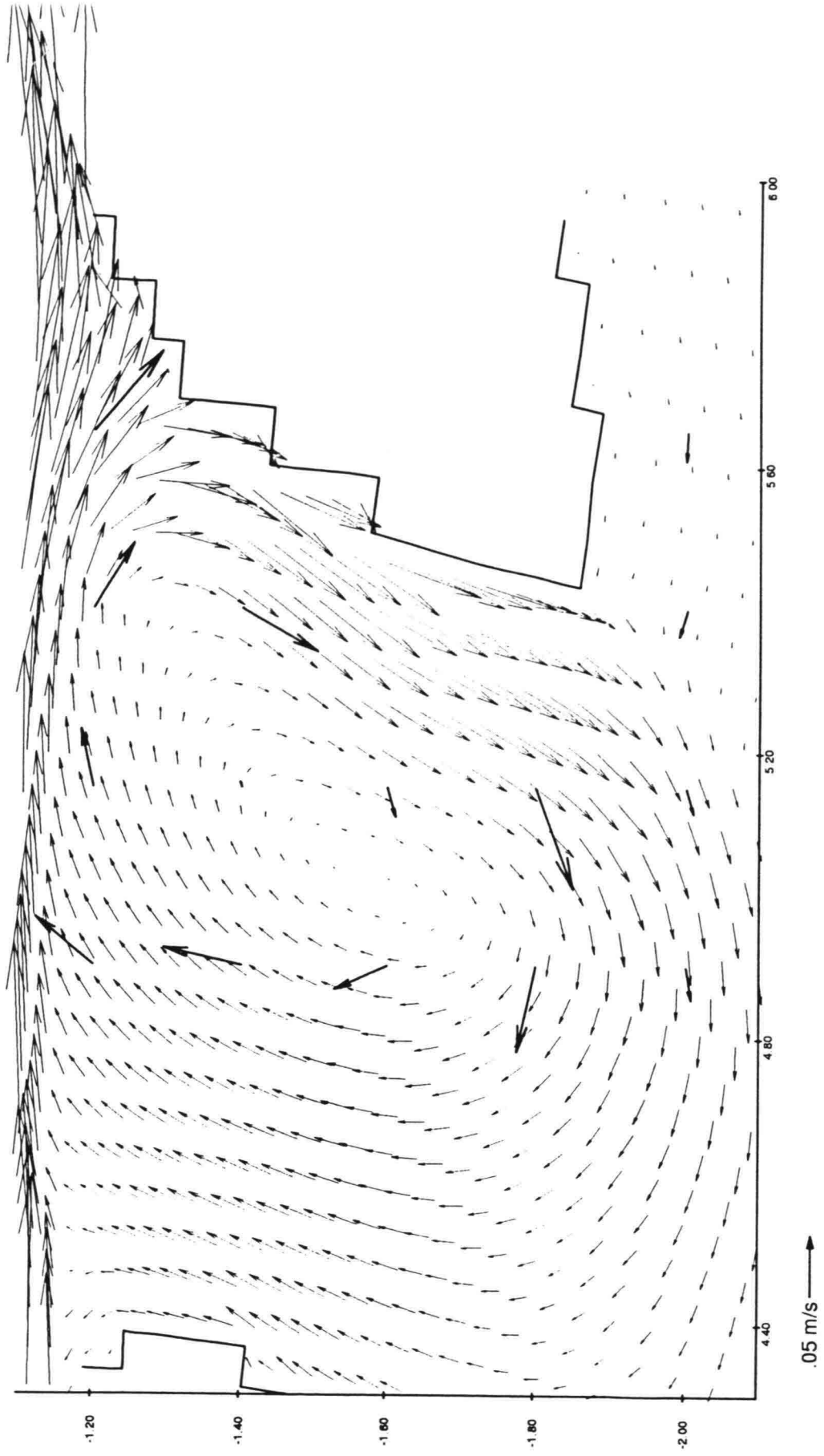

Figure F.17: Velocity vectors at the harbour entrance computed with the standard k-ε model (thin arrows) and PTV measurements (thick arrows) at $\sigma = -.51$. Situation without sill in harbour entrance.

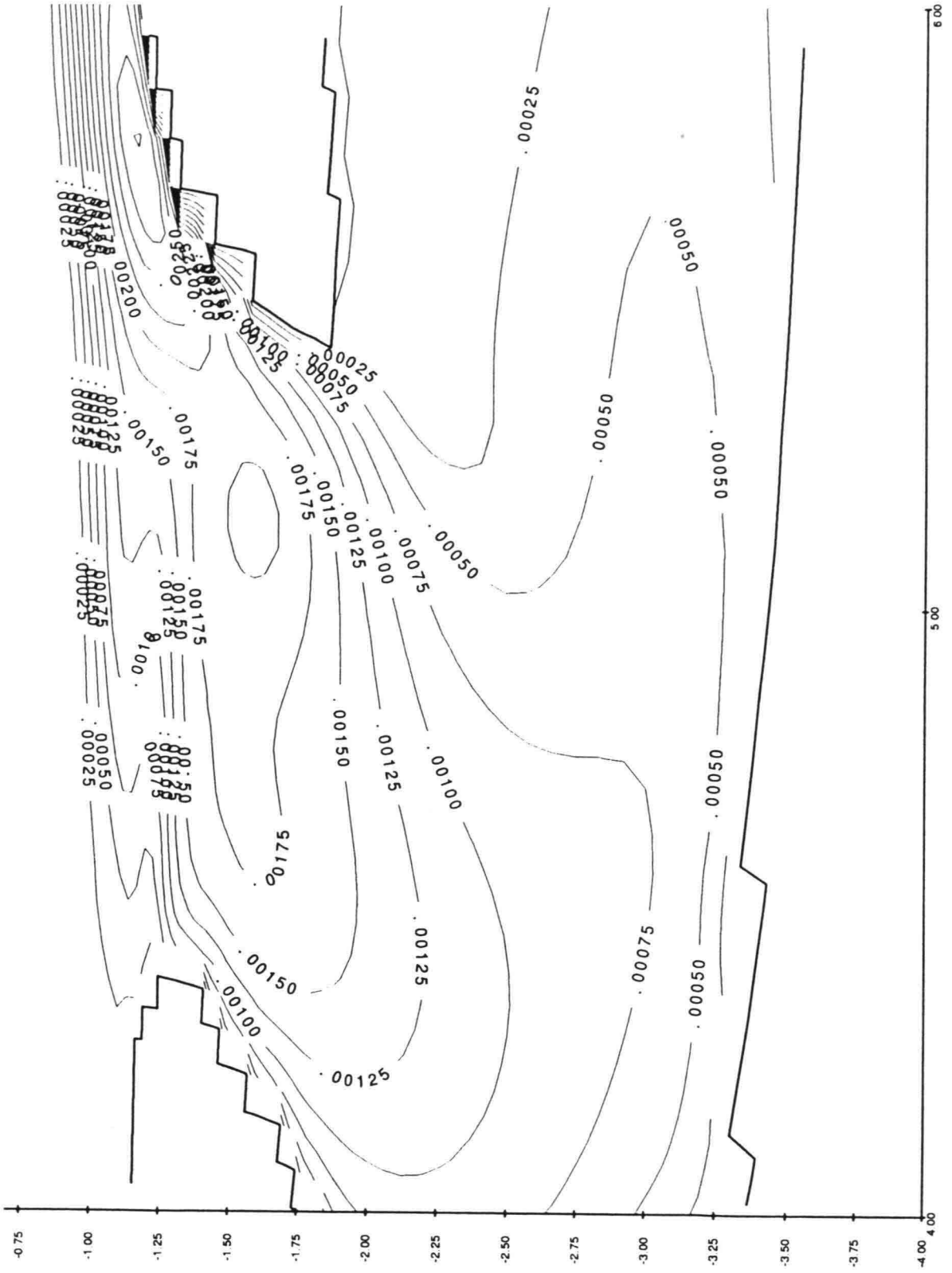

Figure F.18: Horizontal eddy viscosity ν_t^{2D} (m^2/s) computed by the TLS model. Situation without sill in harbour entrance.

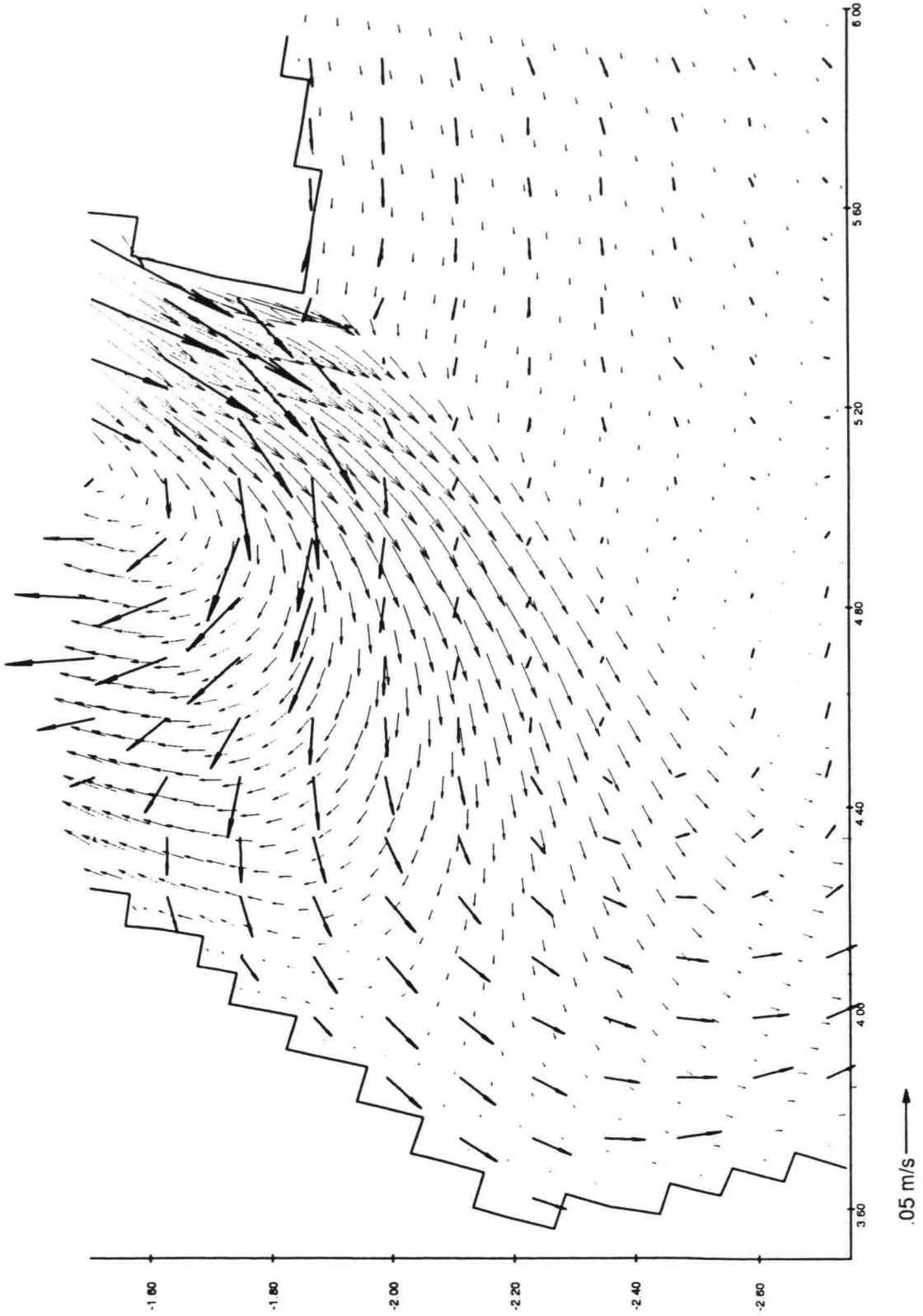

Figure F.19: Velocity vectors in the harbour entrance computed with the TLS model (thin arrows) and PTV measurements (thick arrows) at $\sigma = -.075$ and $\sigma = 0$, respectively. Situation without sill in harbour entrance.

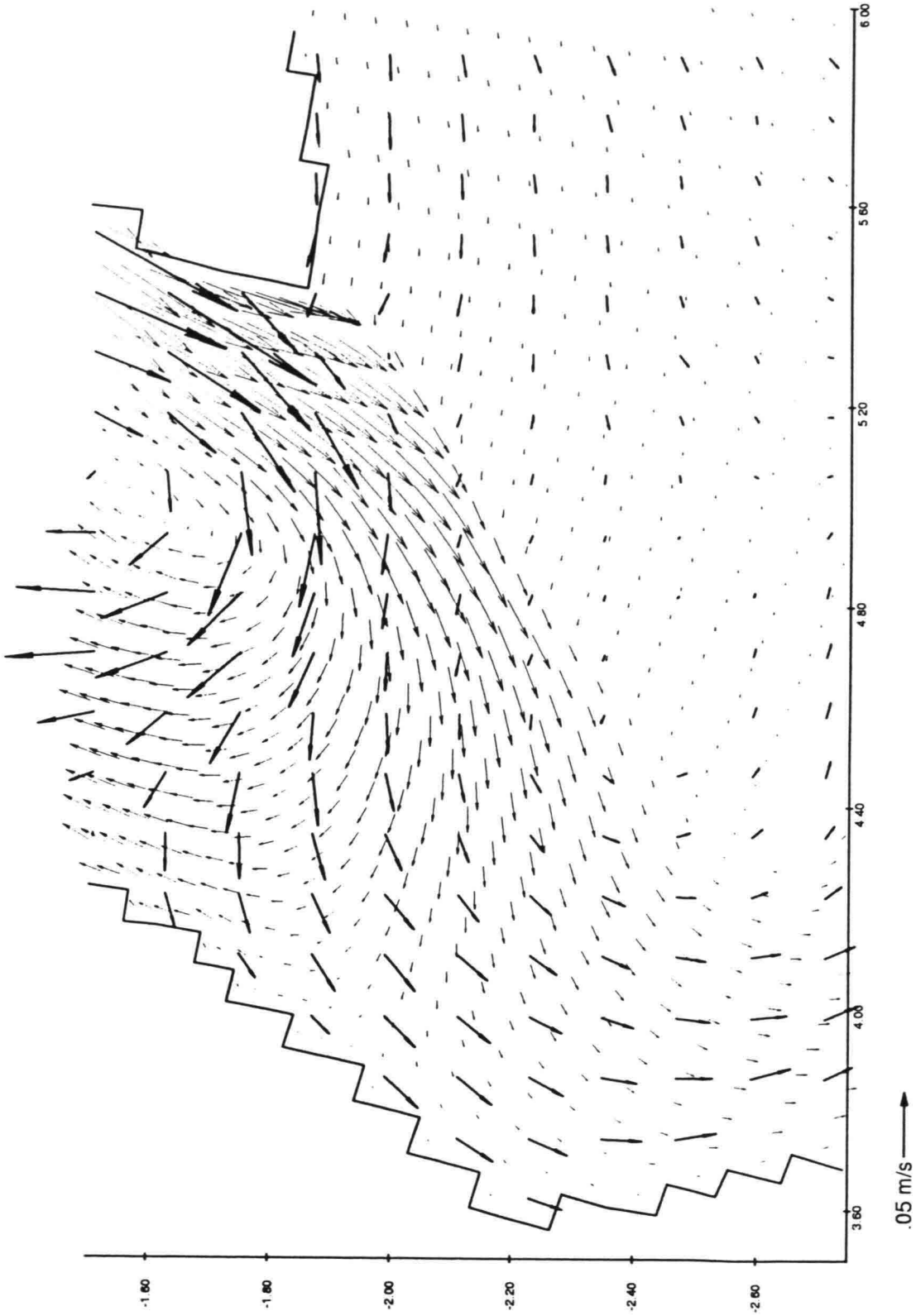

Figure F.20: Velocity vectors in the harbour computed with the standard k-ε model (thin arrows) and PTV measurements (thick arrows) at $\sigma = -.075$ and $\sigma = 0$, respectively. Situation without sill in harbour entrance.

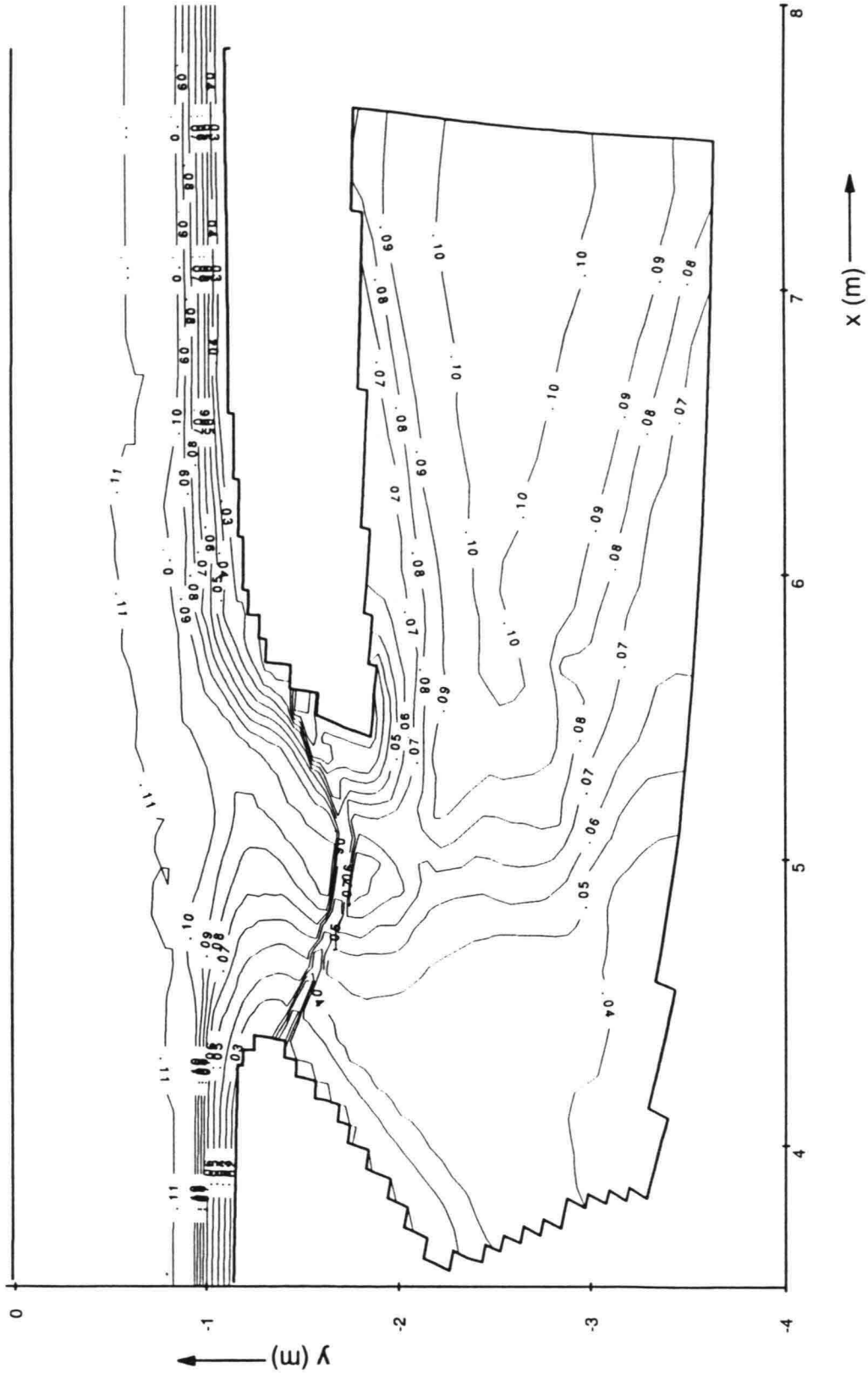

Figure F.21: Isolines of depth, situation with a sill in the harbour entrance.

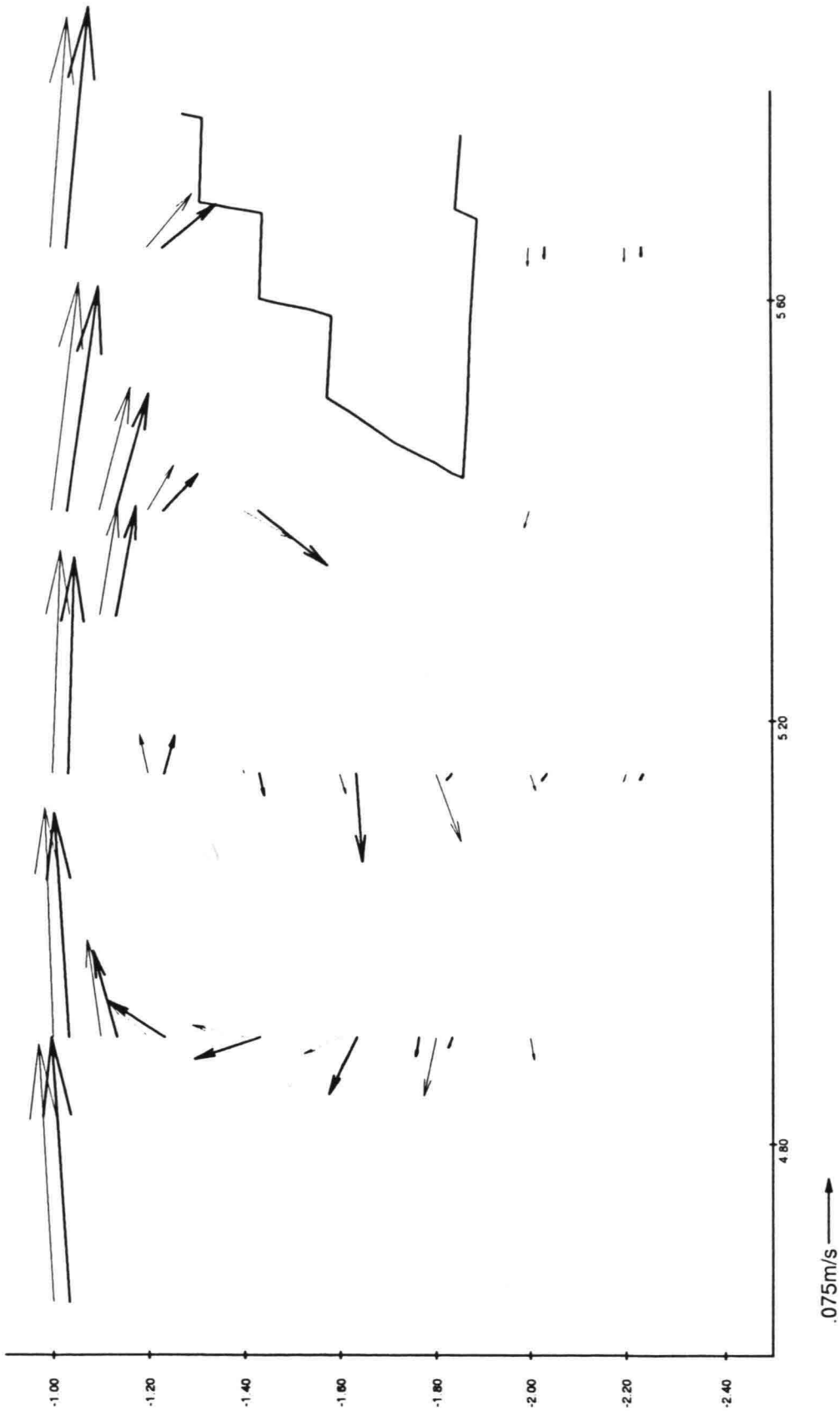

Figure F.22: Comparison of mean velocities at $\sigma = -.51$, obtained with LDA, in situation with (thick arrows) and without (thin arrows) a sill in the harbour entrance.

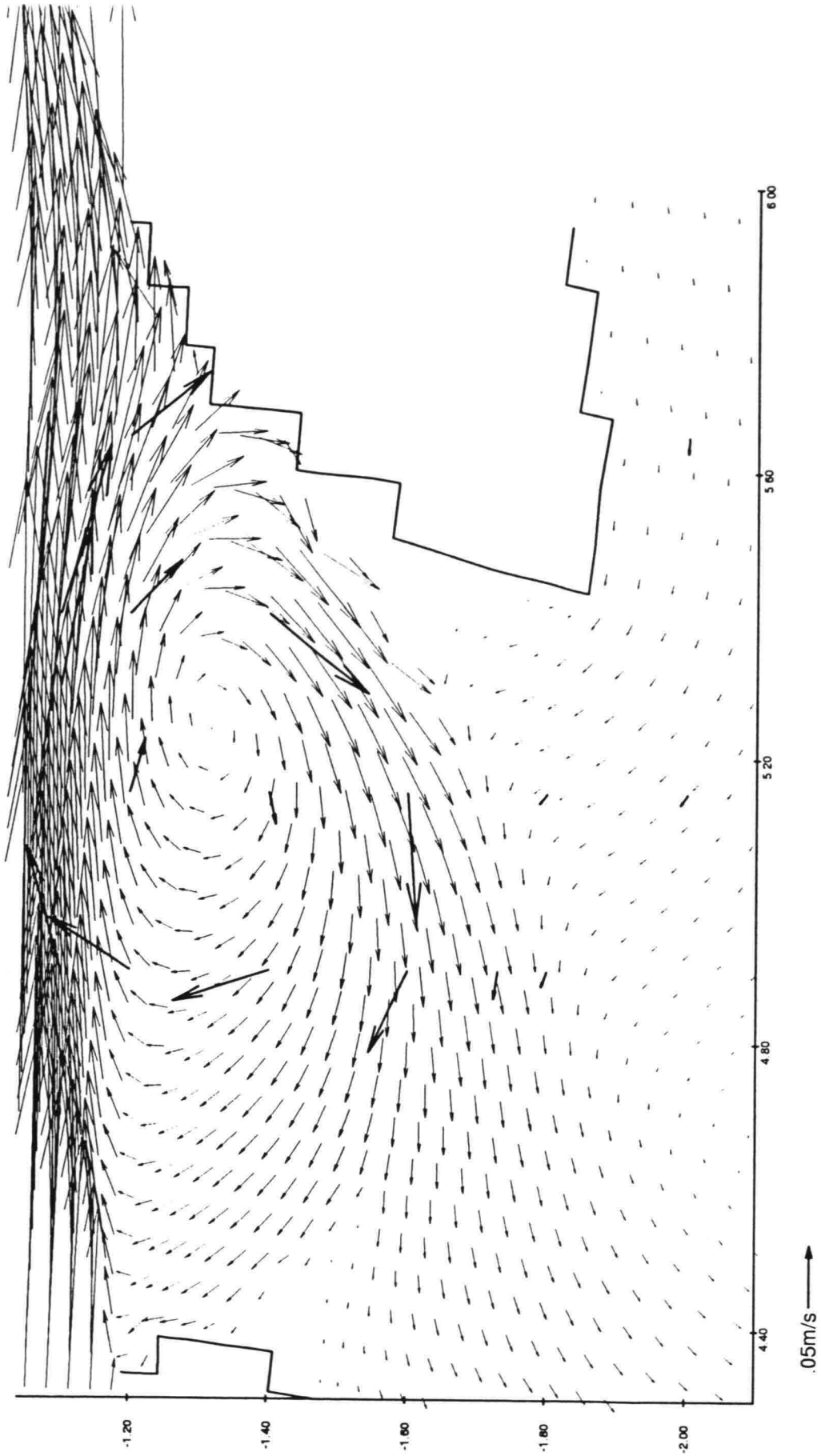

Figure F.23: Velocity vectors at the harbour entrance computed with the TLS model (thin arrows) and LDA measurements (thick arrows) at $\sigma = -.51$. Situation with sill in harbour entrance.

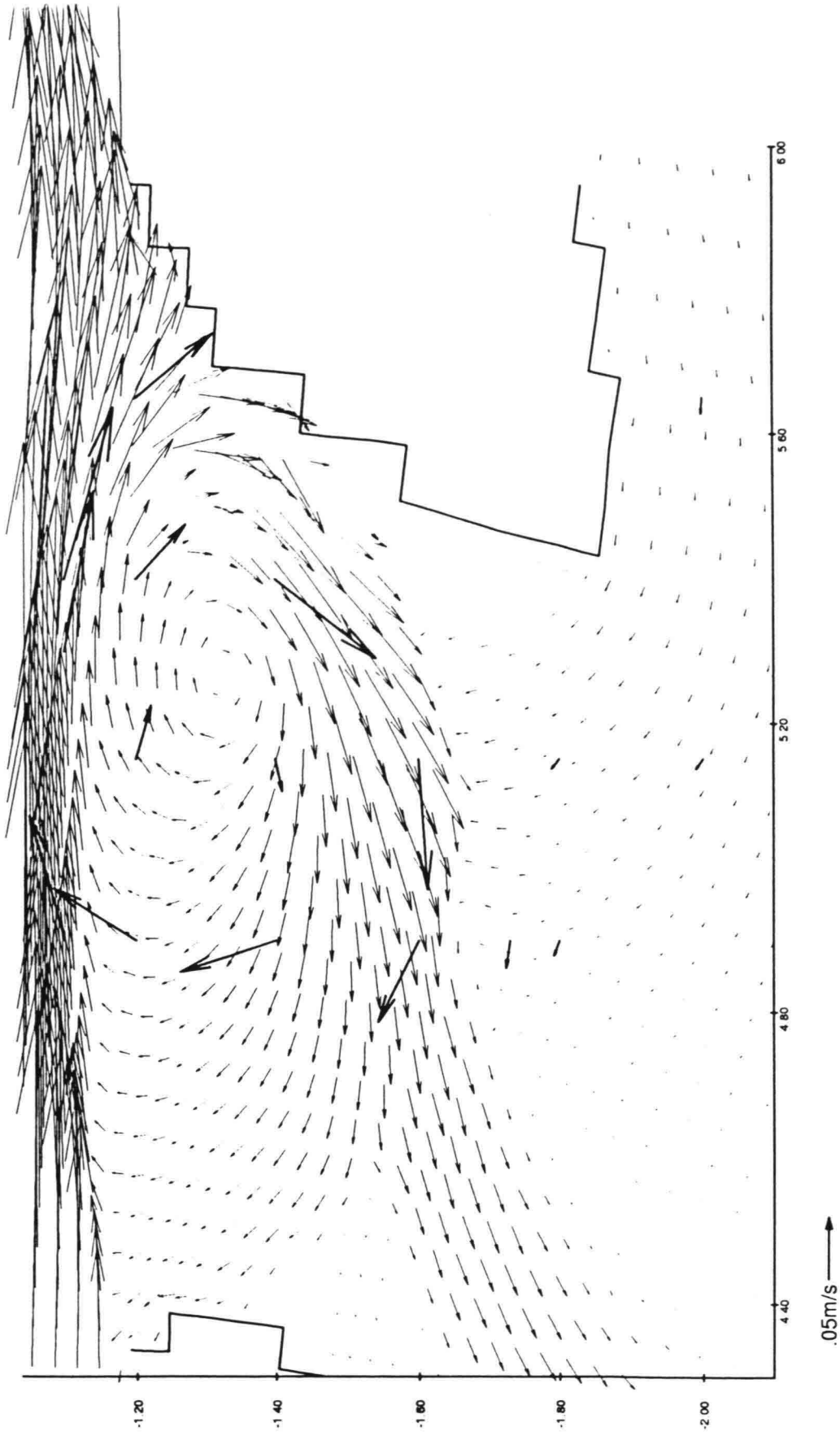

Figure F.24: Velocity vectors at the harbour entrance computed with the standard k-ε model (thin arrows) and LDA measurements (thick arrows) at $\sigma = -.51$. Situation with sill in harbour entrance.

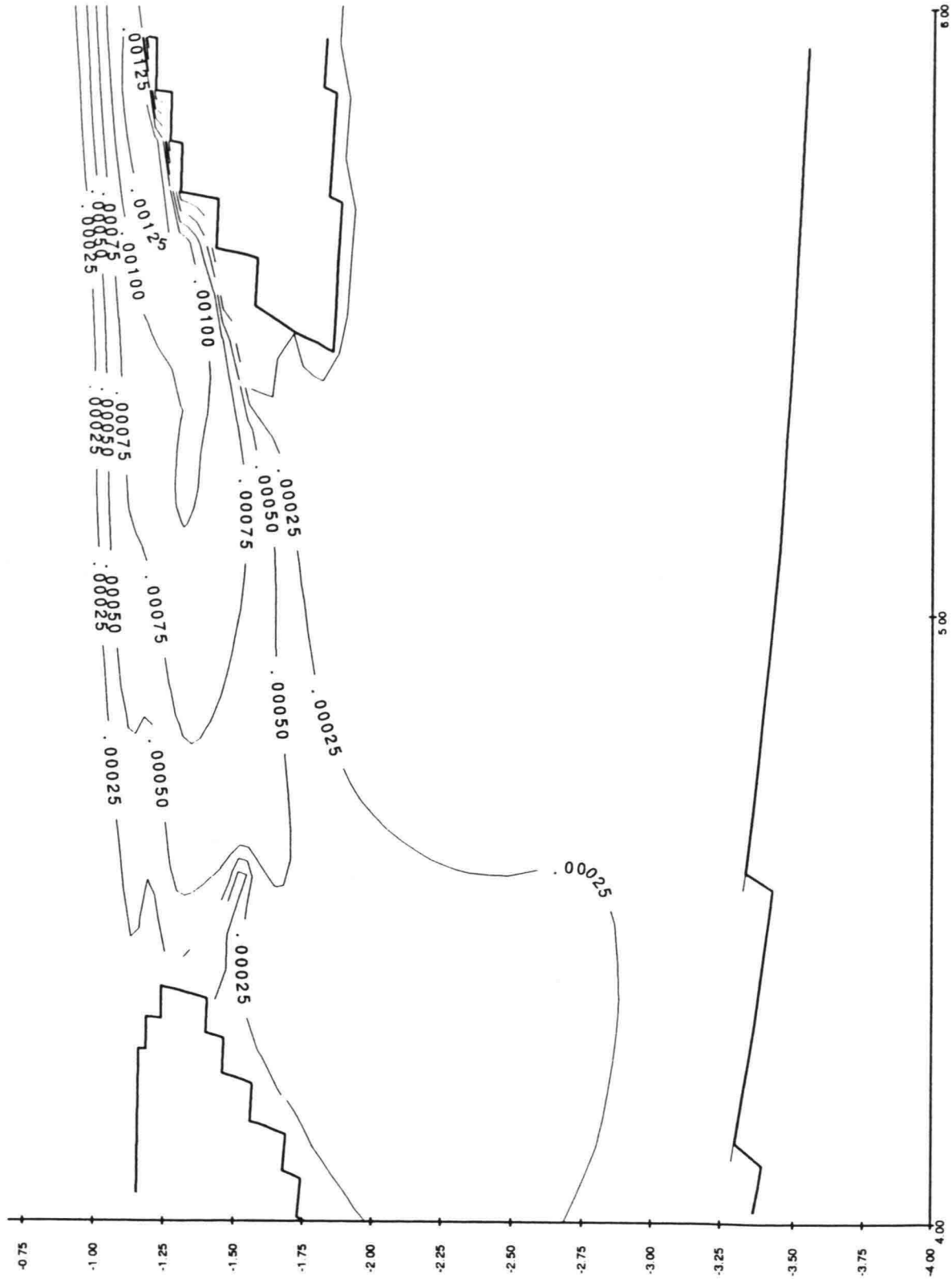

Figure F.25: Horizontal eddy viscosity ν_t^{2D} (m^2/s) computed by the TLS model. Situation with sill in harbour entrance.

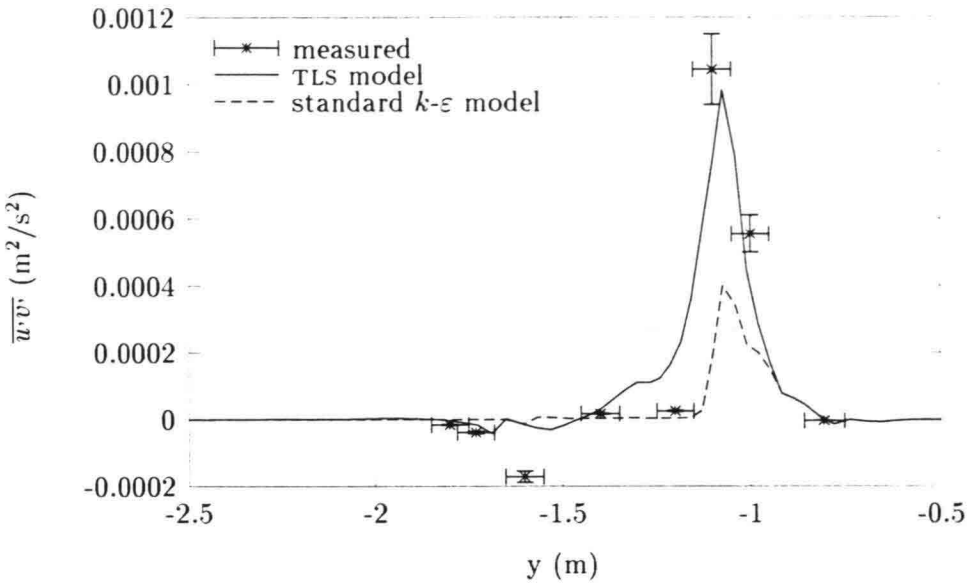

Figure F.26: Reynolds shear stress per unit mass at x=4.9 m and z=-0.05 m. Situation with sill in harbour entrance.

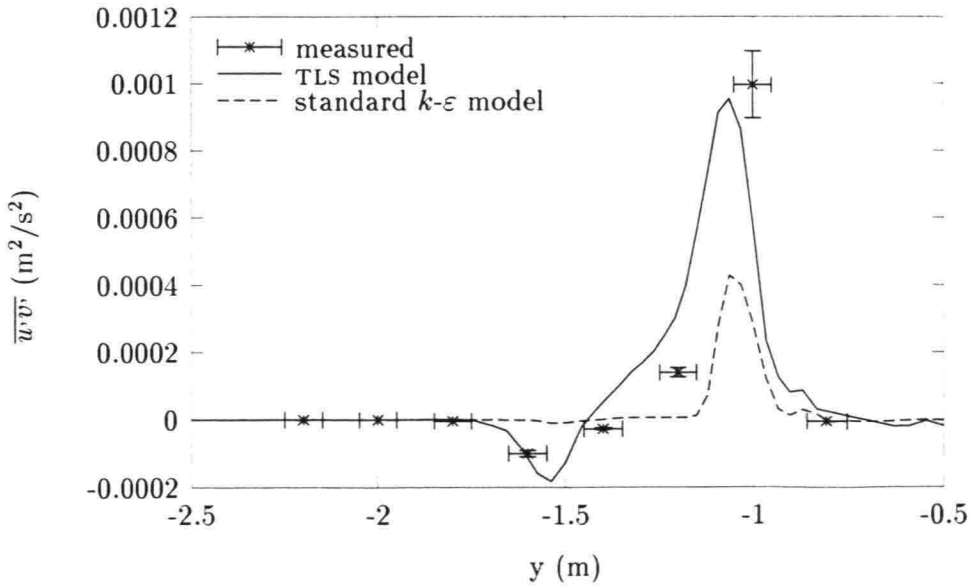

Figure F.27: Reynolds shear stress per unit mass at x=5.15 m and z=-0.05 m. Situation with sill in harbour entrance.

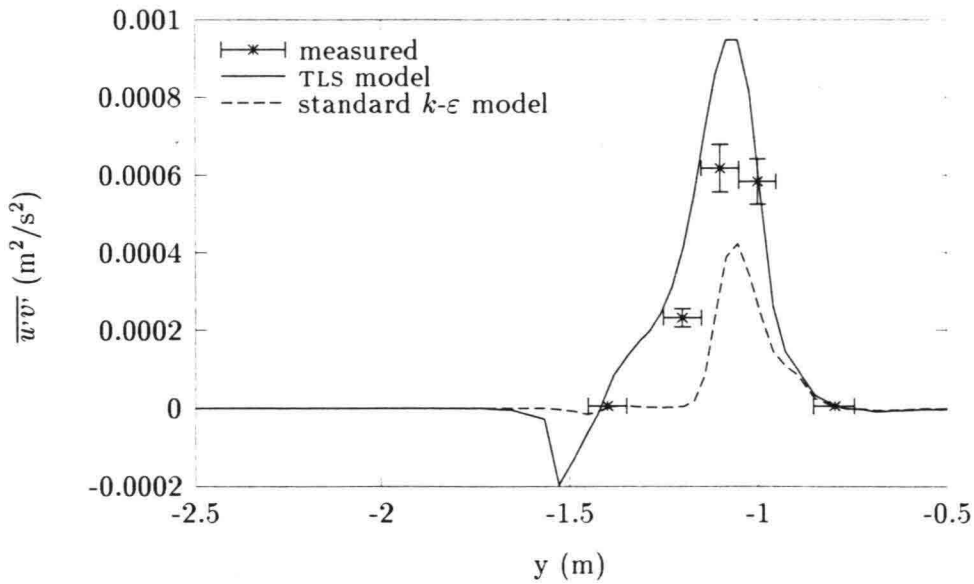

Figure F.28: Reynolds shear stress per unit mass at x=5.4 m and z=-0.05 m. Situation with sill in harbour entrance.